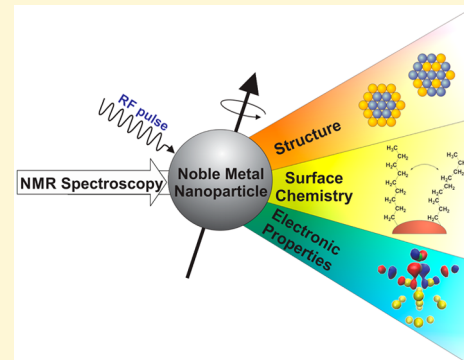


NMR Techniques for Noble Metal Nanoparticles[†]

Lauren E. Marbella and Jill E. Millstone*

Department of Chemistry, University of Pittsburgh, 219 Parkman Avenue, Pittsburgh, Pennsylvania 15260, United States

ABSTRACT: Solution phase noble metal nanoparticle growth reactions are comprised of deceptively simple steps. Analytical methods with high chemical, spatial, and temporal resolution are crucial to understanding these reactions and subsequent nanoparticle properties. However, approaches for the characterization of solid inorganic materials and solution phase molecular species are often disparate. One powerful technique to address this gap is nuclear magnetic resonance (NMR) spectroscopy, which can facilitate routine, direct, molecular-scale analysis of nanoparticle formation and morphology *in situ*, in both the solution and the solid phase. A growing body of work indicates that NMR analyses should yield an exciting complement to the existing canon of routine nanoparticle characterization methods such as electron microscopy and optical absorption spectroscopy. Here, we discuss recent developments in the application of NMR techniques to the study of noble metal nanoparticle growth, surface chemistry, and physical properties. Specifically, we describe the unique capabilities of NMR in resolving hard–soft matter interfaces with both high chemical and high spatial resolution.



1. INTRODUCTION

Nuclear magnetic resonance (NMR) spectroscopy is a transformational molecular characterization tool that requires little perturbation of the analyzed system, while providing exceptional detail about the chemical environments of constituent atomic nuclei. These features make NMR especially well-suited for *in situ* analysis of chemical structure, reactions, and even dynamics in some cases. With this versatility, it is not surprising that NMR analysis has been applied to a wide variety of systems¹ ranging from large biomolecules² to lithium batteries,³ in addition to its daily analytical use in organic synthesis laboratories. The chemical resolution possible using NMR is particularly attractive for characterizing both the formation and final architecture of noble metal nanoparticles (NMNPs). To understand why NMR is promising for these studies one must clarify both what one may want to determine about NMNP systems as well as the unique capabilities of NMR in metallic materials.

Analytical targets in the study of NMNPs range from tracking molecular precursors during NP formation to particle surface reorganization during catalytic reaction and many aspects of particle architecture, electronic properties, and surface chemistry in between. Nanoparticle systems often involve a hard–soft matter interface between the solid surface of the particle core and pendant ligands (species ranging from monoatomic ions to large macromolecules). This interface includes many parameters of interest including surface element composition, ligand shell composition, and ligand shell architecture. However, each of these features is difficult to resolve using classic surface and materials characterization strategies such as electron microscopy or photoelectron spectroscopy techniques.

In this Perspective, we highlight reports, including examples from our laboratory, in which NMR has provided crucial insights into NMNP formation, morphology, and physical properties. First, we briefly outline key NMR concepts in the study of NMNPs including NMR phenomena such as the Knight shift and Korringa behavior. In Section 2, we discuss NMR analyses of NMNP formation and growth, and give examples of studies that monitor either resonances of the ligand (Section 2.1) or NMR-active metal nuclei within the metal precursors (Section 2.2). In the remainder of the Perspective, we discuss final nanoparticle characterization both of the particle itself (Section 3) as well as its resulting physical properties (Section 4).

In each section, we focus on NMR techniques that are generally accessible to the synthetic nanochemistry community. We also consider instrumental and physical limitations of NMR for studying NMNPs where appropriate. At the end of each section, we include results obtained using more advanced NMR equipment and techniques. While these studies may require more expertise to execute, the results obtained are of broad interest and therefore we highlight the method and the results.

1.1. Basic Concepts for Metal Nanoparticle NMR Spectroscopy. While a detailed treatment of NMR theory is outside the scope of this Perspective, the reader is referred to several excellent resources on the long and fruitful study of metals and metal adsorbates using NMR and in particular those by Slichter,⁴ van der Klink and Brom,⁵ and Oldfield and Wieckowski.⁶ Here, we outline selected NMR concepts. The concepts are chosen to be useful for interpreting the results

Received: December 31, 2014

Revised: February 19, 2015

Published: March 11, 2015

[†]This Perspective is part of the *Up-and-Coming* series.

summarized in this Perspective as well as for appreciating the scope of possible contributions using NMR spectroscopy in NMNP systems. In particular, we focus on phenomena unique to NMR of metals, adsorbates on metals, and nuclei at a hard–soft matter interface.

Consider an NMR spectrum of ^{195}Pt nuclei in Pt nanoparticles or a ^1H NMR spectrum of H_2 molecules adsorbed to their surface. In both cases, conduction electrons in the Pt metal will have a dramatic influence on the resulting NMR spectra because of nuclear coupling to conduction electrons at the particle surface (defined as hyperfine coupling). In bulk metals, it is well-known that hyperfine coupling of nuclear spins to the unpaired conduction electrons in the metal results in a dramatic change in NMR frequency termed the Knight shift, K . Observation of the Knight shift was first reported in 1949 when W. D. Knight noticed that the NMR signal for Li, Na, Al, Cu, and Ga metals resonated at a different frequency from that of the same element in a nonmetallic environment (chloride salts).⁷

Like chemical shift, the Knight shift is sensitive to the local electronic environment surrounding the nucleus, and the magnitude of the shift is a sensitive probe of the electronic structure of metals, semiconductors, and superconductors.⁸ Therefore, exciting experiments such as probing the change from molecular to metallic electronic structure in NMNPs is possible using NMR techniques. Further, metallic properties can be studied by evaluating the Korringa behavior of materials through NMR measurements. In the Korringa relation,⁹ K is related to the temperature, T , at which the NMR measurement is performed and the longitudinal relaxation time constant, T_1 , of the material where K^2TT_1 is a constant. As a result, T_1 and T^{-1} display a linear relationship with one another.¹⁰ NMR nuclei that exhibit this temperature correlation with T_1 suggest metallic electronic structure within the material analyzed. Both the slope of the temperature dependent relaxation as well as the magnitude of the Knight shift can give information about the evolution of particle electronic structure as a function of particle size, shape, composition, and surface chemistry.⁸

Surface chemistry is particularly interesting because NMNPs prepared by wet chemical techniques are often capped with organic molecules. By combining the unique impact of metal conduction electrons on ligand nuclei with traditional NMR spectroscopy techniques, NMR investigation of these capping ligands can provide detailed insight into properties of the particle core (e.g., electronic structure, atomic composition, or compositional architecture) as well as important aspects of its ligand shell including ligand identity, arrangement, and dynamics.

For each nucleus observed, the measured resonance will be influenced by both “macroscopic” and “microscopic” forces acting on it.¹¹ At the macroscopic level, the homogeneity and strength of the applied magnetic field, molecular tumbling, and magnetic susceptibility of the material can each influence observed spectral features. Many NMR techniques have been developed to either mitigate the impact of these macroscopic effects or to leverage them as in solid state NMR (ssNMR). “Microscopic” factors include the electronic environment of the nuclei as well as the influence of neighboring nuclear and electronic spin interactions. These microscopic interactions may be deduced from several spin-1/2 NMR figures of merit, including chemical shift, line width, relaxation times, and chemical shift anisotropy (CSA).

For a given chemical environment, several of these spectroscopic parameters may be influenced simultaneously. Further, because NPs incorporate components from both molecular chemistry (e.g., organic capping ligands) and solid phase materials (e.g., metallic core), methods may be used or combined from both traditional solution phase NMR characterization as well as more advanced ssNMR techniques. In order to ascertain how different spectral features arise in spectra obtained from these techniques, we begin by discussing a traditional solution phase spin-1/2 1D NMR spectrum and focus on a single nuclear site, j . In a typical spectrum of a small molecule, sharp resonance lines of chemical shift, $\delta_{\text{iso},j}$, are observed at a frequency (in ppm) that is proportional to the external magnetic field, B_0 .

$$\omega_{0,j} = \gamma_j B_0 (1 + \delta_{\text{iso},j}) \quad (1)$$

In eq 1, $\omega_{0,j}$ is the chemically shifted Larmor frequency for site j , and γ_j is the gyromagnetic ratio of nucleus j . Here, the direction of the external magnetic field is in the z -direction of a three-coordinate axis. Each nuclear site may exhibit a unique chemical shift as the result of differences in chemical shielding.¹² The chemical shielding interaction is composed of both a diamagnetic and a paramagnetic contribution that results in frequency shifts.¹³ The magnitude of the chemical shielding depends on the molecular electronic structure and the orientation of the molecule with respect to B_0 .¹⁴ In solution, rapid reorientation of the small molecule with respect to B_0 allows it to sample all orientations on a time scale that averages the CSA and dipole–dipole coupling to zero. This averaging results in an *isotropic* chemical shift and sharp resonance lines in the solution phase NMR experiment (Figure 1A).

However, a static ^{13}C ssNMR spectrum of the same small molecule shows a broad powder pattern. This apparent loss in spectral features is due to spin interactions such as CSA and dipole–dipole coupling which are not averaged out in the solid state because of restricted molecular motion. In theory, the effects of both CSA and dipole–dipole coupling can be

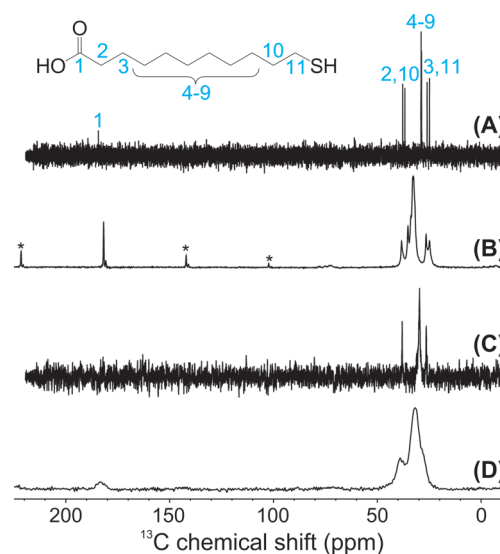


Figure 1. 1D ^{13}C NMR spectra of 11-mercaptoundecanoic acid in (A) D_2O , (B) the solid state with $\text{MAS} = 5$ kHz and ^1H decoupling = 80 kHz, (C) D_2O appended to Au NPs ($d = 2.2$ nm), and (D) the same NPs in the solid state. Asterisks in (B) denote spinning sidebands from moderate MAS speeds = 5 kHz.

removed from ssNMR spectra via magic-angle spinning (MAS) in combination with high power decoupling (Figure 1B).

When small molecules are attached to a metal nanoparticle, they are at the interface between solution and a solid support. Therefore, if the same small molecule depicted in Figure 1A is appended to a AuNP and the same 1D ^{13}C NMR spectrum is recorded, several spectral differences will be apparent: line broadening of the resonances is observed, the chemical shift may be altered, and some resonances may disappear completely (Figure 1C). These changes become more dramatic when the particles are dried to a solid state (Figure 1D). For spin-1/2 nuclei, such as the ^{13}C solution phase spectra in Figure 1C, the spin interactions that arise from being in a more “solid-like” environment can be briefly explained as a reintroduction of anisotropic spin interactions. For example, CSA can arise from the different frequencies associated with each different orientation of the same molecule with respect to B_0 . If the molecule does not reorient at a rate greater than the absolute magnitude of the CSA (which can be the case when attached to a nanoparticle substrate because of restricted molecular motion), inhomogeneous line broadening is observed in the NMR spectrum.

Likewise, dipole–dipole coupling can also be a source of line broadening and is the through-space interaction between the induced magnetic moments of neighboring spins. Measuring dipole–dipole coupling constants can provide detailed information about the structure and arrangement of ligands attached to NMNPs in both the solid and solution phase. For example, the effect of dipole–dipole coupling on nuclear spin relaxation results in nuclear Overhauser effects that can be measured by NMR and provide information on the distances between nuclei (termed nuclear Overhauser effect spectroscopy (NOESY)). Using specialized pulse sequences, spin interactions can be selectively reintroduced to learn about the molecular environment of nanoparticle capping ligands, including the degree of crystallinity, orientation, and supramolecular architecture.

Depending upon the size of the underlying nanoparticle, molecular tumbling of pendant ligands may be greatly reduced. The attenuation of molecular tumbling rates via attachment to relatively large particle surfaces results in a reintroduction of CSA and dipole–dipole coupling spin interactions as discussed above. Changes in the magnitude of spin interactions (e.g., by fixing molecules in close proximity or near a metal center) can also influence the spin–lattice relaxation (or longitudinal relaxation, T_1) and spin–spin relaxation (or transverse relaxation, T_2). Here, T_1 is defined as the time constant for spins to reach thermal equilibrium in the presence of B_0 . Similarly, T_2 is the time constant that describes the dephasing of spin polarization associated with single quantum coherences in the transverse plane. In particular, T_2 is related to the observed NMR full width at half-maximum (fwhm) by the following equation:

$$\text{fwhm} = \frac{1}{\pi T_2} \quad (2)$$

Another spin interaction that will be mentioned is the quadrupolar interaction. Quadrupolar nuclei are nuclei with spin $> 1/2$ and can have either integer or half-integer spins. In these cases, the nucleus has an electric quadrupole moment which is coupled to the surrounding electric field gradient, producing the quadrupolar interaction. Quadrupolar interactions are commonly characterized by nuclear quadrupole

coupling constants. It is important to note that, in many systems, especially solids where molecular motion is restricted, the magnitude of quadrupolar coupling can surpass the magnitude of the dipole–dipole coupling interactions, producing NMR lineshapes that are dominated by quadrupolar interactions.¹⁵ Here, we will focus mainly on the quadrupolar interaction as it applies to deuterium NMR spectroscopy, where deuterium is spin-1 and has a relatively small quadrupole moment.

2. NUCLEAR MAGNETIC RESONANCE CHARACTERIZATION OF METAL NANOPARTICLE FORMATION AND GROWTH

During the formation of NMNPs, both chemical change and phase transformations occur. Following the evolution of molecular precursors into a final NP solid phase requires methods that can capture chemical and physical transformations in real time with molecular resolution. NMR approaches to study growth have employed a broad range of techniques, as well as combined NMR with other analytical methods such as thermogravimetric analysis (TGA), Raman spectroscopy, and differential scanning calorimetry (DSC). To study NMNP growth, both the nuclei of NP ligands as well as the metal nuclei themselves can be monitored.

2.1. NMR Observation of Nanoparticle Ligand Resonances during Synthesis.

First, we consider the use of NMR to monitor the chemical environment, reaction rates, and dynamics of ligands used in NMNP syntheses. One nanochemical reaction mechanism that has benefited significantly from NMR analysis is the two-phase Brust–Schiffman synthesis.¹⁶ Briefly, this synthesis involves the transfer of aqueous HAuCl_4 into an organic solvent such as toluene via a “phase transfer agent” such as tetraoctylammonium bromide (TOAB), and a thiolated ligand (RSH) solubilized in the organic phase. A reducing agent such as $\text{NaBH}_4(\text{aq})$ is introduced and thiolate-terminated AuNPs are produced (diameter $d \approx 1\text{--}5 \text{ nm}$).¹⁶ In general, the mechanism of formation is thought to begin by an initial reduction of Au(III) species to Au(I) via oxidation of RSH ligands. The resulting species are then fully reduced by NaBH_4 and particle nucleation is induced. On the basis of dynamic light scattering (DLS) measurements and the sensitivity of the final product size to metal:RSH ratio, it has been thought that metal–sulfur bond formation occurred after RSH addition and that polymeric Au(I) -thiolate species were the active precursor to thiolate-capped NPs produced via the two-phase approach.

Using 1D ^1H NMR analyses of precursors at various Au:RSH ratios, Lennox and co-workers found that, after thiol addition, Au(III) is indeed reduced to Au(I) and that RSH is oxidized to the disulfide but that there was no evidence of metal–sulfur bond formation prior to the introduction of NaBH_4 (Figure 2A,B).¹⁷ Instead, Lennox postulates the formation of $\text{TOA}^+ - [\text{AuX}_2]^-$ species and supports this assignment via chemical shift differences in the TOA^+ resonances after the addition of HAuCl_4 and its transfer to the organic phase. TOA^+ proton resonances (protons on the carbons adjacent to the nitrogen) were consistent with fast anion exchange between coordination of TOA^+ to $[\text{AuX}_2]^-$ and Br^- . Similar metal–surfactant precursors were subsequently identified for analogous Ag and Cu two-phase NP syntheses.¹⁷

This work led to a proposed “inverse micelle mechanism” by Tong and co-workers¹⁸ where the metal ion coordination complex is sequestered in an inverse micelle of TOAX ($X = \text{Br}^-$

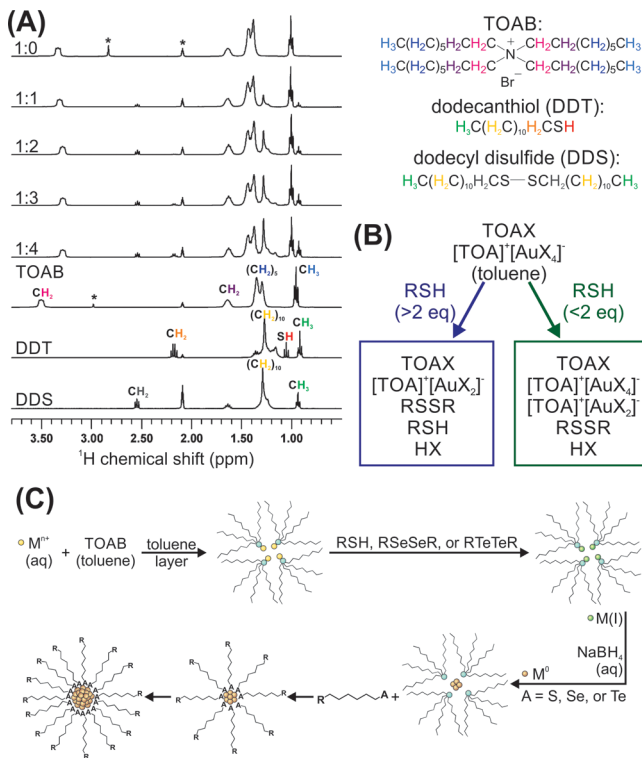


Figure 2. (A) ¹H NMR spectra of TOAX + TOA⁺–[AuX₄][–] titrated with increasing equivalents of dodecanethiol from top to middle as well as spectra of pure TOAB, dodecanethiol, and dodecyl disulfide free in solution. (B) Diagram describing possible nanoparticle precursors in the first two steps of a two-phase Brust–Schiffman synthesis based on spectra in (A). (C) Proposed scheme for nanoparticle formation based on similar NMR analyses to (A) and Raman spectroscopy. (A) and (B) adapted with permission from ref 17. Copyright 2010 American Chemical Society. (C) adapted with permission from ref 18. Copyright 2011 American Chemical Society.

or Cl[–]). Both the size of the micelle and the chemical environment inside play crucial roles in the ultimate size and stability of AuNPs formed, even in the absence of an RSH ligand. Tong et al. support this mechanism via both NMR and synthesis experiments. Using 1D ¹H NMR, the authors follow the water resonance and show chemical shift values consistent with sequestration of water inside a TOAX micelle¹⁹ or other supramolecular architecture. Further, the TOA⁺–[AuX₂][–] precursor could be prepared in high purity according to a literature procedure, eliminating the need for RSH reduction of TOA⁺–[AuX₄][–]. Then, the thiolated capping ligand could be added post-NaBH₄ addition and indistinguishable particles could be obtained for Au, Ag, or Cu cores (Figure 1C).

This particle formation pathway differs from observations in a one-phase synthesis,^{20,21} involving the same reagents with the exception of the phase transfer agent TOAB, which is no longer needed and typically omitted. In the one-phase synthesis, metal–sulfur bonds are observed before NaBH₄ addition, which is consistent with results from our own laboratory. Cliffel and co-workers studied the one-phase aqueous synthesis of tiopronin-capped AuNPs and used a combination of ¹H NMR, TGA, matrix assisted laser desorption ionization mass spectrometry (MALDI-MS), and pair distribution function (PDF) analysis to identify precursor species.²² The authors showed that a possible precursor to AuNPs in the tiopronin synthesis was a Au(I)–thiolate tetramer with distinct optical

signatures, and these observations are consistent with theoretical predictions of “pre-nucleation” species.^{23,24} Interestingly, features of the Au(I)–thiolate tetramer are also present in the final colloid ($d = 2\text{--}3$ nm), suggesting that the intermediates may also be present as capping moieties on the particle surface. Studies of analogous syntheses using phosphine-based ligands have been studied using ³¹P ssNMR spectroscopy and indicate that Au(I) ligand complexes also form prior to reduction and subsequent particle formation.²⁵

Taken together, these NMR studies suggest that there are fundamental differences between the formation pathways of small NMNPs ($d = 1\text{--}5$ nm) synthesized by one-phase and two-phase methods, despite the seemingly similar protocols. These distinctions are important contributions to establishing well-controlled, easily tailored, and high yielding NMNP syntheses.

Another canonical NMNP synthesis studied by solution phase ¹H NMR is the citrate reduction of Au(III) at elevated temperature (~100 °C), commonly referred to as the Turkevich²⁶ or Frens²⁷ method. In this synthesis, citrate acts as both a reducing agent for Au(III) as well as a capping ligand for the final NPs. By altering either the solution pH (and presumably the speciation of both the Au precursor and/or the reduction potential of the citrate) or the ligand to metal ratio, the final particle size and size distribution can be modified ($d \sim 10$ to 100 nm). In order to correlate variations in precursor chemistry with particle products, Bruylants and co-workers monitored the Turkevich synthesis at constant citrate:Au(III) ratio (5:1) at various pH values (pH = 3, 4.5, 7, 9, and 12) using a combination of UV–visible absorption and NMR spectroscopy as a function of time.²⁸

In this work, the authors identified that the narrowest particle size distribution was obtained from reactions performed at pH 7. At pH 7, a majority of the citrate ligand was found by ¹H NMR to be deprotonated ($pK_a = 3.1, 4.8, 6.4$) and the Au species was present as [AuCl₂(OH)]₂[–] as determined by UV–visible spectroscopy. Under these conditions, dicarboxyacetone appeared in the ¹H NMR spectrum within 1 min of reaction initiation, where dicarboxyacetone is the primary oxidation product of citrate and itself a reducing agent. However, when the reduction of Au cations is performed with dicarboxyacetone alone, particle size distribution increases, indicating that the reaction is sensitive to kinetics and/or progresses by a different route than when using citrate.

In addition to the appearance of the dicarboxyacetone peak, a new, broad peak at the base of the free citrate peaks was observed. 2D ¹H–¹H correlation spectroscopy (COSY) analysis indicated that the peaks were consistent with citrate in fast exchange with two different chemical environments on the NMR time scale. When the diffusion coefficients of the various citrate peaks were measured by diffusion ordered spectroscopy (DOSY), citrate aggregates containing Au atoms (either Au(I) or Au(0); not yet known) were observed.²⁸ These Au–citrate aggregates are consistent with the supramolecular metal–ligand assemblies proposed to explain nucleation and growth of AuNPs using the Turkevich approach.²⁶

NMR techniques may also be used to follow NMNP syntheses that use a gas reduction approach. In one example, Chaudret et al. characterize AuNP formation ($d = 4.7 \pm 0.9$ nm) using a combination of solution phase and ssNMR techniques to monitor the CO(g)-reduction of a gold precursor in the presence of amine-functionalized capping ligands.²⁹

Solution phase ^1H NMR measurements showed that the reaction shared mechanistic features with the one-phase Brust–Schiffrin synthesis. For example, after combining hexadecylamine (HDA) with Au(I)Cl(tetrahydrothiophene) (THT), a Au(I)Cl–HDA coordination complex is formed. Resulting spectral features support this assignment including the disappearance of the triplet from the protons on the carbon adjacent to the amine group, coincident appearance of new resonances that correspond to Au(I)Cl–HDA, and the appearance of resonances that correspond to free THT. After reduction of the Au(I)Cl–HDA complex by CO(g), AuNPs are formed and were characterized using ssNMR MAS techniques (to mitigate spectral line-broadening due to the increasing size of the NP core). ^{13}C ssNMR spectroscopy indicated that, after reduction, 1,3-dihexadecylurea was formed via carbonylation of HDA. As a result, the final particle product was terminated with a binary ligand shell composed of both amine and carbamide ligands.

NMR has also been used to investigate how early NP nuclei may be stabilized but continue to grow. Studying an IrNP system, Finke and co-workers used a combination of ^1H and ^2H NMR spectroscopy to understand how ionic liquid media are able to stabilize transition metal NPs by monitoring the ionic liquid chemistry during synthesis.³⁰ The authors found that Ir(0) NPs ($d = 2.1$ nm) reacted with imidazolium-based ionic liquids in order to form surface-bound carbenes, suggesting that chemical reaction of the solvent can create molecular stabilizers for the growing particle surface. Solvent and other reaction byproducts have been implicated as stabilizing agents in other NP syntheses as well. For example, Polte et al.³¹ have shown that borate byproducts may stabilize Au and Ag NPs on the time scale of hours during and after their formation when using NaBH₄ as a reductant in the absence of other ligand reagents.

In addition to determining the chemical evolution of ligand precursors and their role in particle growth, NMR has also been used to probe the role of capping ligands in the emergence of particle shape. For example, Gordon and co-workers used ^1H – ^{13}C cross-polarization (CP)-MAS NMR spectroscopy to determine the surface composition of poly(vinylpyrrolidone) (PVP, MW = 29 kDa)-capped Ag–Pt nanocubes and octahedra ($d = 6$ –8 nm) before catalytic evaluation.³² As may be expected, when more Ag precursor is added to the synthesis, more Ag is incorporated into the final particle architecture. For each new composition, dramatically different ^1H – ^{13}C CP-MAS NMR spectra are observed, each of which deviates from the spectrum of pure PVP. Upon increasing Ag addition to the final particle, ^{13}C resonances that correspond to hydrocarbons and amines begin to appear. At the same time, characteristic ^{13}C resonances of PVP, specifically those from the 5-membered ring in the polymer repeat unit, disappear. Combined, these results suggest that Ag promotes bond cleavage to form hydrocarbon and amine fragments from the original PVP ligand—an interesting observation of changes in ligand chemistry initiated by the forming particle itself. Importantly, these spectroscopic changes in ligand chemistry as a function of Ag addition correlated not only with alloy composition but also with overall alloy shape, suggesting that metal–PVP reactions may bias surface growth rates and influence the final particle morphology.

2.2. NMR Observation of Metal Nuclei during Synthesis. In addition to observing ligand chemistry during the steps of NMNP synthesis, NMR-active metal nuclei allow direct observation of metal precursor behavior as well. Unfortunately,

while 100% naturally abundant, the large quadrupole moment of the ^{197}Au nucleus precludes direct observation via NMR with current methods, although coupling to heteroatoms, such as ^{31}P , has been reported.³³ Luckily, other metal nuclei have more favorable NMR properties, such as ^{195}Pt and $^{109/107}\text{Ag}$. While Ag NMR holds promise for understanding silver NP precursor chemistry, both isotopes suffer from low sensitivity because of low gyromagnetic ratios and therefore generally require specialized low-gamma probe hardware for NMR observation. Further, Ag nuclei typically exhibit extremely long T_1 values (on the order of hours) making data acquisition time-consuming.

Despite these difficulties, understanding the magnetic resonance properties of inorganic silver compounds, many of which are NP precursors, is an area of active research³⁴ and the applications to NP synthesis are beginning to be explored. For example, Liu, Saillard, and co-workers have used a combination of NMR spectroscopies (^1H , ^2H , ^{31}P , ^{77}Se , and ^{109}Ag), UV–vis, ESI-MS, FTIR, TGA, elemental analysis, single crystal X-ray diffraction, and density function theory (DFT) to monitor the conversion of Ag(I) salts into hydride-centered Ag clusters (number of atoms ranging from 7 to 10) and larger Ag NPs ($d = 30$ nm).³⁵ Here, ^{109}Ag NMR was used to locate the hydrogen atom within the Ag clusters. Figures of merit such as the coupling constant between Ag and H were consistent when measured either by ^1H NMR or ^{109}Ag NMR ($J_{\text{H}-\text{Ag}} = 39.4$ Hz and $J_{\text{Ag}-\text{H}} = 39.7$ Hz, respectively) indicating a robust structure assignment.

To date, the majority of work studying NMNP formation via NMR of metal nuclei has focused on Pt and specifically on Pt precursors. One of the first studies was reported by Murphy and co-workers and used a combination of solution phase ^{195}Pt , ^1H , and ^{13}C NMR to determine the dynamics of ligand exchange between $[\text{PtCl}_4]^{2-}$ and poly(amidoamine) (PAMAM) dendrimers during dendrimer-mediated PtNP synthesis.³⁶ ^{195}Pt NMR, in particular, was used to identify the speciation of the metal precursor upon binding to the dendrimer as well as track Pt precursor uptake into the template branches. The goal of the study was to understand the chemical environment of the Pt(II) precursor (starting material = K₂PtCl₆) before reduction to Pt(0) by NaBH₄ in the presence of either generation 2 (G2-OH) or generation 4 (G4-OH) PAMAM dendrimers. In both G2-OH and G4-OH cases, the ^{195}Pt NMR signal intensity assigned to $[\text{PtCl}_4]^{2-}$ decreased, while new peaks arose as Cl[−] ligands were replaced by nitrogen-containing sites from within the dendrimer. On the basis of chemical shift analyses, the number and type of nitrogen substitution could be deduced, with each successive amine substitution leading to a chemical shift change of −261 ppm and each successive amide substitution leading to a chemical shift change of −333 ppm.

In addition to chemical shift distribution, the total Pt(II) signal could also provide information about the sample. For example, in the case of G2-OH, 50% of the total ^{195}Pt NMR signal disappeared during uptake, and this decrease was attributed to a black Pt(0) precipitate that formed during the course of uptake (~2 days). In the G4-OH system no precipitate is observed over 10 days, but the ^{195}Pt NMR signal intensity is attenuated by ~80%, indicating that the discrepancy may be due to signal dephasing of Pt nuclei in areas of restricted molecular motion such as inside the dendrimer or from aggregation of more than one dendrimer. Overall, the authors found that Pt(II) uptake, speciation, and reactivity was a complex result of the dendrimer architectures, correlating

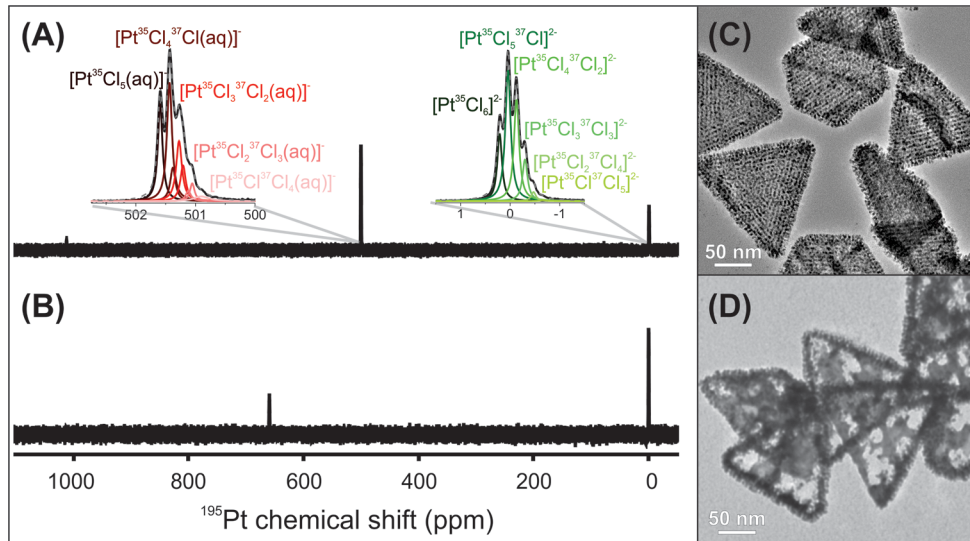


Figure 3. ¹⁹⁵Pt NMR spectra of Pt(IV) precursor solutions at pH 1.8 (A) and 8.6 (B). Corresponding TEM images of particle motifs of Pt deposition on Au nanoprisms substrates when Pt(IV) precursor solution pH is 1.8 (C) and 8.6 (D). Insets in (A) show ¹⁹⁵Pt NMR chemical shift assignments for monosubstituted species $[\text{PtCl}_5(\text{aq})]^-$ (left) and $[\text{PtCl}_6]^{2-}$ (right) using isotopologue analysis at $B_0 = 14.1$ T. In the case of monosubstitution, isotopomers could also be resolved upon peak fitting. Black lines represent experimental spectra, colored lines represent the peak fits for each isotopologue and/or isotopomer, and dashed gray lines represent the sum of the peak fit. Adapted with permission from ref 37. Copyright 2014 American Chemical Society.

with both the impact of ligand exchange about the Pt(II) center as well as the sterics of the dendrimer as a whole.

Recently, we have studied the role of Pt(IV) speciation on reaction pathways in Pt-containing, mixed metal NP syntheses. Specifically, we examined the influence of Pt(IV) speciation on the deposition of Pt metal onto colloidal AuNP substrates (Figure 3).³⁷ Here, Pt(IV) speciation was controlled by adding NaOH to the H_2PtCl_6 precursor solution which we used as a strategy to control the extent of Pt hydrolysis that occurs in aqueous solutions of H_2PtCl_6 . We then monitored the resulting ligand substitution of the Pt center as a function of pH via solution phase ¹⁹⁵Pt NMR spectroscopy.

Monitoring ligand substitution of these complexes via ¹⁹⁵Pt NMR is particularly attractive because chemical shift assignment can be supported by isotopologue analysis of the pendant chloride ligands. In this analysis, the isotopologue distribution of ³⁵Cl/³⁷Cl species in the $[\text{PtCl}_6]^{2-}$ and $[\text{PtCl}_x\text{L}_y]^{n-}$ (where L = H_2O or OH^-) can be extracted from deconvolution of NMR peaks (Figure 3A, insets). Specifically, at high field strengths ($B_0 = 14.1$ T), ³⁷Cl substitution leads to an upfield shift of ~ 0.17 ppm.³⁸ The relative populations of isotopologues in the spectra directly correlate with the natural abundance of the respective chlorine isotopes. Further, for monosubstituted $[\text{PtCl}_x\text{L}_y]^{n-}$ species, resolution of both ³⁵/³⁷Cl isotopologues and isotopomers is possible (isotopomers are represented by the same color in the peak fitting in Figure 3). This analysis provides both a spectroscopic fingerprint for Pt(IV) complexes in solution as well as a relative quantification of various Pt species in solution.³⁹

Ultimately, Pt(IV) speciation was found to correlate well with final NP morphologies, and the pH of the original Pt(IV) precursor solution was a reliable method to modulate this speciation parameter. Particularly interesting was the impact of speciation at high precursor solution pH. At pH 8.6, 67% of the Pt(IV) complexes are $[\text{PtCl}_6]^{2-}$ and 33% are the monosubstituted $[\text{PtCl}_5(\text{OH})]^{2-}$. When Pt(IV) precursor solutions at this pH are used for Pt deposition on the AuNP substrates, the

majority of AuNPs are oxidized via a galvanic replacement mechanism and the synthesis results in the formation of framelike Au–Pt alloy nanostructures (Figure 3D). Conversely, when Pt(IV) precursor solution pH is low, reduction of the metal cation occurs primarily via externally added reducing agent oxidation (in this case, ascorbic acid), as evidenced by lack of oxidation in the Au nanoprisms substrate (Figure 3C). The difference in Pt(IV) reduction pathway is consistent with previous electrochemical studies of $[\text{PtCl}_6]^{2-}$ in water, which find that OH^- substituted halide complexes are more readily reduced.⁴⁰ Therefore, controlling Pt(IV) speciation (and thereby metal precursor reduction potential) is a synthetic handle with which to mediate whether Pt(IV) reduction will occur via oxidation of the small molecule reducing agent (leading to deposition *on top of* the existing particle substrate) or through oxidation of existing NPs in solution (leading to cage-like, hollow, or “frame” nanostructures). These insights provide important mechanisms for tunability in the synthesis of Pt-containing NP products which are of interest in many applications including fuel cells⁴¹ and data storage.⁴²

Overall, the literature suggests that unprecedented, molecular-scale information can be gained by using NMR to monitor the chemical conversion of NP precursors in both the solution and the solid phase, under diverse reaction conditions, and for several different metal identities. These insights should lead to a deeper understanding of NMNP synthesis mechanisms and ultimately provide a robust foundation for future NP synthesis design.

3. NUCLEAR MAGNETIC RESONANCE CHARACTERIZATION OF NOBLE METAL NANOPARTICLES

In addition to providing critical insights into the formation of NMNPs, NMR techniques may also be used to understand several aspects of the final nanoparticle architecture. NMR stands out here, because it is able to resolve molecular architectures at the surface of the solid phase nanoparticle. In

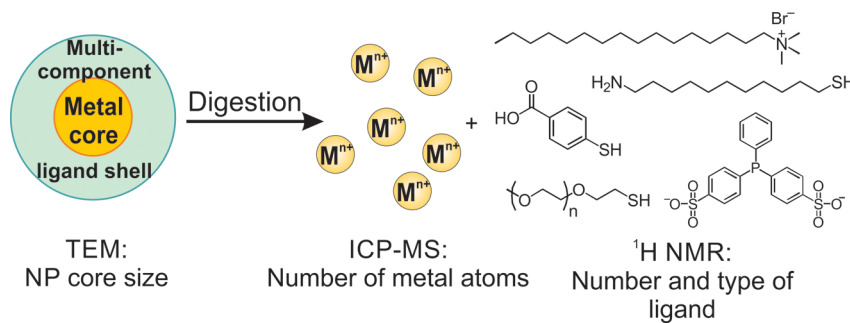


Figure 4. General procedure to analyze the number and type of ligands present on a nanoparticle. Nanoparticle core size and total metal atom concentration are used together to determine the nanoparticle concentration. Adapted with permission from ref 54. Copyright 2015 American Chemical Society.

this section, we discuss the use of NMR techniques to elucidate features of both the nanoparticle core and the nanoparticle ligand shell with high spatial and chemical resolution.

3.1. Metal Nanoparticle Surface Chemistry: Small Molecule Ligand Shells. *3.1.1. Ligand Identity and Quantity.* An important aspect of ligand shell characterization is monitoring the process and final products of ligand exchange. These studies require the ability to evaluate both ligand identity as well as quantity. NMR spectroscopy is particularly well-suited for these requirements, because of the chemical resolution offered by chemical shift and the direct relationship between NMR signal integration and spin population. Indeed, solution phase ^1H NMR spectroscopy has been used to quantify the type and amount of ligands on quantum dots and metal oxide nanoparticles,^{43–46} and similar approaches have been used to assess the relative ratios of ligands in mixed monolayer systems appended to NMNPs.^{47–50} However, in order to achieve quantitative results, NMNP cores typically must be digested due to line broadening effects that become increasingly problematic at larger particle sizes (*vide supra*).^{51,52} Perhaps more importantly, with all bulk ligand quantification strategies to date (including those using NMR), the accuracy of ligand density values is fundamentally limited by the size distribution of the nanoparticle cores analyzed.

Using NMR to monitor ligand exchange in real time was performed without particle digestion to gain information on ligand exchange. At very small particle sizes (generally <200 atoms), ligand exchange can be monitored on intact particles with relatively well-resolved NMR spectra due to the rapid tumbling in solution, similar to that of small molecules. Yarger and co-workers used solution-phase ^1H NMR to observe ligand exchange on triphenylphosphine (PPh_3)-capped AuNPs ($d = 1.8$ nm) with both $d_{15}\text{-PPh}_3$ or $\text{Au(I)}(d_{15}\text{-PPh}_3)\text{Cl}$ in CD_2Cl_2 .⁵³ Under ambient conditions, both $d_{15}\text{-PPh}_3$ and $\text{Au}(d_{15}\text{-PPh}_3)\text{Cl}$ showed similar kinetics with ligand exchange rate constants (0.17 and 0.20 min^{-1} , respectively) extracted from time-dependent ^1H NMR spectroscopy. In both cases, $\text{Au(I)}(\text{PPh}_3)\text{Cl}$ was removed from the particle surface and replaced with the incoming ligand. Further analysis with ^{31}P NMR of the tethered PPh_3 groups was consistent with Au(0) and/or Au(I) phosphine complexes, indicating that Au–phosphine complexes, rather than simply PPh_3 , was the capping ligand in these systems.

Recently, we have exploited the quantitative capabilities of ^1H NMR spectroscopy to describe both the identity and absolute quantity of ligands before and after ligand exchange on commonly used pseudospherical AuNPs ($d = 13$ and 30 nm).⁵⁴

The method is a widely applicable approach to quantify ligand shell compositions using a combination of transmission electron microscopy (TEM), inductively coupled plasma mass spectrometry (ICP-MS), and ^1H NMR spectroscopy (Figure 4). The accuracy associated with this methodology was verified by comparison of ligand quantities between several techniques using specialized ligands designed specifically to be analyzed via several approaches. First, a selenol-functionalized ligand was synthesized and appended to the AuNP surface. After particle digestion, the sample ligand solution was analyzed by two methods: ^1H NMR as described in Figure 4 and ICP-OES (optical emission spectrometry) for analysis of Se atom concentrations. Using multiple modes of statistical analysis to compare values obtained from these two techniques, both ^1H NMR and ICP-OES were found to yield statistically equivalent ligand values within a 95% confidence interval. Quantification can also be performed by the addition of a high purity internal standard with a known number of protons and concentration, such as dimethylmalonic acid (DMMA), or by using ERETIC (electronic reference to access *in vivo* concentrations) techniques⁵⁵ for ligand concentration evaluation in a single spectrum, eliminating the need to construct a calibration curve. To demonstrate this point, we also conducted ^1H NMR ligand quantification experiments using DMMA. Similar to the comparison with ICP-OES, we found that both approaches showed statistical agreement (no difference within 95% confidence interval).

Using the approach outlined in Figure 4, we found that ligand addition mechanisms are strongly influenced by intermolecular interactions within the ligand shell itself. We expect these findings will have implications for both routine surface characterization of AuNPs as well as for generating highly tailored surface chemistries that optimize particle functionality in applications such as multivalent biomolecular interactions or catalytic reactions.

3.1.2. Ligand Shell Morphology. Under conditions where the ligand is still appended to the nanoparticle surface, spatial information, including the average local chemical environment of the ligands as well as overall ligand architectures adopted on-particle, may be studied. The observation of ligand shell architectures is a particularly exciting application of NMR spectroscopy, because resolution of ligand shell morphology is difficult to observe with traditional materials characterization techniques (*vide supra*).

Two of the fundamental driving forces behind the formation of various ligand shell morphologies are chemical interactions between individual ligands and chemical interactions between ligands and the nanoparticle surface. A variety of NMR

techniques can be used to probe these interactions. For example, 1D and 2D ^1H high resolution (HR)MAS NMR techniques showed the presence on $\pi-\pi$ stacking between aromatic ligands appended to a AuNP surface (orientation of the $\pi-\pi$ stacking with respect to the particle surface was not resolved).⁵⁶ One may also systematically monitor ligand position by using either the particle surface itself⁵⁷ or site-specific paramagnetic lanthanide labels,^{58,59} both of which act as a spectroscopic ruler by dephasing resonances closest to the unpaired electron (for more information about distance-dependent NMR signal dephasing using a variety of methods, the reader is referred to the work of Solomon⁶⁰ and Bloembergen⁶¹). Both strategies have been used to assess parameters such as protein–nanoparticle binding sites on specific residues⁵⁷ and molecular position-mapping of organic capping ligands,^{58,59} respectively.

Although limited distances ($\sim 5 \text{ \AA}$) can be measured with solution phase NMR techniques, detailed structural information on various ligand shell architectures and arrangement can still be ascertained. Recently, Stellacci and co-workers presented a ^1H NMR method to determine ligand shell morphologies by predicting ^1H chemical shift trends as a function of ligand shell composition (also measured with ^1H NMR, but with digested particles) in combination with NOE cross peak patterns (Figure 5).⁶² Using this method, the authors were able to

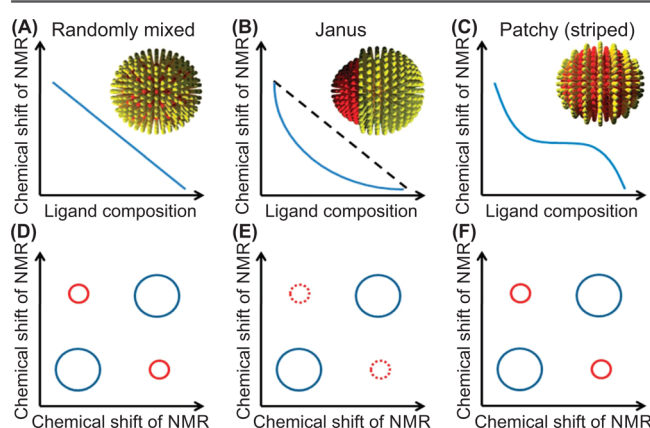


Figure 5. Ligand shell arrangements and morphologies can be assessed by combining solution phase ^1H chemical shift with NOE analysis. (A), (B), and (C) represent the predicted chemical shift patterns as a function of ligand composition. (D), (E), and (F) represent the predicted NOE cross-peak patterns as a function of randomly mixed, Janus, and patchy ligand shell morphologies. Reproduced with permission from ref 62. Copyright 2012 Nature Publishing Group.

determine the difference between randomly mixed, Janus, and patchy ligand shell morphologies on AuNPs ($d = 2\text{--}5 \text{ nm}$) capped by binary mixtures of aromatic and aliphatic molecules. Further, ^1H NMR line narrowing of specific ligand resonances provided spectroscopic evidence for structural defects associated with particular morphologies.

To extract architectural information from this combination of 1D ^1H NMR spectra and NOE patterns, two important experimental conditions must be met. First, the binary ligand shell composition must be tunable across all composition space (i.e., from 0 to 100% of each ligand). This control is needed in order to observe the changes in chemical shift associated with the ligand mixtures as shown in Figure 5A–C. Second, the ^1H NMR resonances of the constituent ligands must be well-

resolved to observe the cross-peaks shown in Figure 5D–F (i.e., distinct and preferably very well-resolved from one another on the chemical shift spectrum). The first limitation can be overcome as a more robust understanding of ligand shell chemistry evolves, with a significant amount of progress attributed to the information gained from NMR studies (vide supra). Additionally, the need to study mixed ligand systems with well-resolved resonances can be mitigated by moving to higher field strengths and/or other observable nuclei with larger chemical shift ranges than traditional ^1H NMR, such as ^{31}P or ^{13}C .

Additional spatial information on nanoparticle ligand shells can be gained by using advanced ssNMR techniques, such as rotational echo double resonance (REDOR).⁶³ Strong dipolar couplings between neighboring nuclei lead to broad NMR lines in the solid state that can be averaged out with MAS. Due to long-range order observed in solids, selective reintroduction of dipolar couplings with REDOR allows for the measurement of much longer distances between nuclei ($\sim 25 \text{ \AA}$) than in the solution phase, in which dipolar couplings are averaged out by molecular tumbling.

One example of this technique was used to distinguish between bilayer formation via a disulfide linkage vs a hydrogen bonding interaction with important implications for cysteine-mediated protein binding to AuNP surfaces. Here, Gullion and co-workers used $\{^1\text{H}\}^{13}\text{C}\{^{15}\text{N}\}$ REDOR to selectively reintroduce heteronuclear dipolar couplings on uniformly labeled ^{13}C , ^{15}N L-cysteine and L-cystine capped-AuNPs ($d = 6.6 \text{ nm}$).⁶⁴ REDOR measurements along with ^1H – ^{13}C CP-MAS NMR analysis showed that the thiol-group of the L-cysteine molecule was chemisorbed to the Au surface and formed an initial ligand layer. Thiol anchoring of the initial monolayer exposed charged amino and carboxyl groups on the zwitterionic L-cysteine, to which a second L-cysteine layer coordinated via hydrogen bonding. ^1H MAS analysis indicated that the outer layer of L-cysteine molecules interacting with the chemisorbed inner layer exhibit large amplitude motion about the carbon–carbon bonds.⁶⁵ Comparison to L-cystine-functionalized AuNPs indicated that L-cysteine was not absorbed as the disulfide analogue. While these results are significant for protein-attachment strategies to AuNPs, their more important impact is in establishing REDOR as a powerful approach to resolve long-range interactions within the NMNP ligand shell, analogous to structural detail that has been transformative in structural biology.

3.1.3. Ligand Shell Structural Dynamics. In addition to probing the identity, quantity, and arrangement of ligands on metal NP surfaces, NMR techniques are also useful to probe variations in structure (e.g., as a function of temperature) and dynamics of the NP ligand shell with atomic site resolution within the ligand.⁶⁶

For example, by simply measuring the ^{13}C NMR chemical shift values of ligand resonances appended to a nanoparticle, the crystallinity of alkanethiol ligand shells can be estimated. This strategy takes advantage of ^{13}C chemical shifts that are particularly sensitive to trans- and gauche-conformational changes for ligands tethered to solid surfaces. Under MAS conditions in the solid state, all-trans conformations for interior methylenes resonate at 33–34 ppm and gauche conformations appear between 28–30 ppm.⁶⁷ As expected, in solution a dynamic equilibrium between trans and gauche conformations is typically observed and leads to an averaged ^{13}C chemical shift of 29–30 ppm, consistent with chemical shift averaging

observed in other equilibrium processes monitored by NMR. More detailed information on alkyl chain dynamics, relative molecular mobilities, and the degree of crystallinity can be measured with a combination of ^{13}C and ^1H T_1 relaxation measurements, $^{13}\text{C}-^1\text{H}$ heteronuclear dipolar dephasing experiments (Figure 6B), and 2D $^{13}\text{C}-^1\text{H}$ wide-line separation ssNMR experiments.⁶⁸

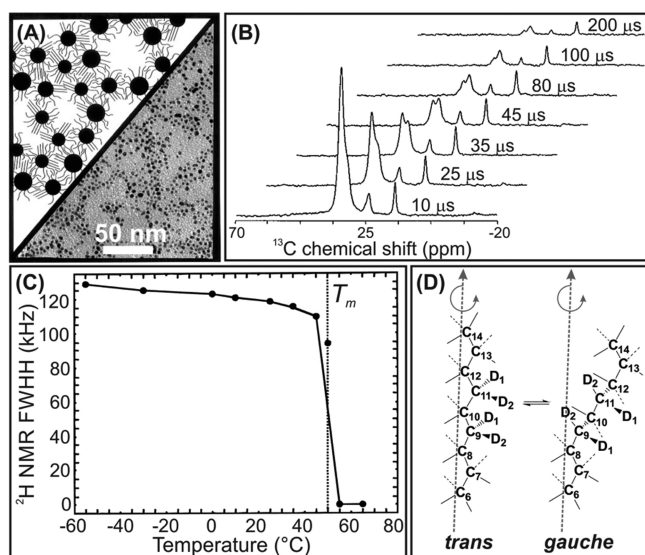


Figure 6. (A) Scheme of possible nanoparticle interactions and corresponding TEM image of octadecanethiol-terminated AuNPs and (B) $^{13}\text{C}-^1\text{H}$ dipolar dephasing measurements of the NPs shown in (A). (C) Correlation of static ^2H NMR lineshapes with phase transitions measured with DSC (T_m). (D) Scheme of trans and gauche methylene conformers in equilibrium as measured by ^2H NMR spectroscopy. (A) and (B) adapted with permission from ref 68. Copyright 1996 American Chemical Society. (C) and (D) adapted with permission from ref 69. Copyright 1997 American Chemical Society.

Using the strategies above, chain ordering trends on AuNPs ($d = 2\text{--}5 \text{ nm}$) as a function of alkyl chain length have been evaluated.⁶⁸ In all cases, the thiol moiety is anchored to the AuNP surface, which is evident from NMR signal dephasing at ^{13}C positions adjacent to the thiol. When the alkanethiol chain length is $< \text{C}_8$, the ligand shells show dynamics similar to that of the solution phase (N.B. this does not imply rapid exchange with solution phase ligands), indicating that a high population of gauche conformers is present at short chain lengths. On the other hand, when the alkanethiol chain length is increased to C_{18} , the ligand shell displays a high degree of conformational order from large-amplitude motion about the chain axes in a mostly trans conformation. The increased conformational order was proposed to be a result of chain intercalation in the solid state with neighboring particles (Figure 6A).

Surprisingly, ssNMR analyses also revealed a non-negligible population of gauche conformers concentrated at chain termini in C_{18} thiol-capped AuNPs, a detail that was not apparent from FTIR analysis alone. While also a bulk measurement of the average, NMR has the distinct advantage of providing ^{13}C chemical shift resolution of specific carbon sites and different electronic environments along the alkane chain. Further, phase transitions observed via DSC corresponded to reversible alkyl chain disordering, as determined by variable temperature (VT) $^1\text{H}-^{13}\text{C}$ CP-MAS experiments. These results were later

confirmed and expanded by Lennox and co-workers using a combination of DSC, FTIR, and ^2H ssNMR.⁶⁹

In addition to crystallinity and chain ordering trends in alkanethiol-capped AuNPs, the influence of terminal-alkyl functional groups on these architectures was studied using similar methods. Both conformational order and thermal stability have been studied for several chain lengths and functional groups including alcohols,⁶⁸ carboxylic acids,⁷⁰ phosphonic acids,⁷¹ and sulfonic acids.⁷¹ In general, the authors found that hydrogen bonding imparted a higher degree of conformational order and thermal stability compared to methyl-terminated analogues.

Solid state NMR techniques were used to resolve not only interactions at the ligand–solvent interface but also to provide important insight into ligand–particle bonding at the hard–soft matter interface. To describe in similar structural detail the metal–sulfur binding motif present in AuNPs, Lennox, Reven, and co-workers investigated the Au–SR interaction using ssNMR techniques for both long- (C_{14}) and short-chain (C_4) alkanethiols.⁷² Site-selective ^{13}C isotopic labeling was used to enhance and resolve the ^{13}C NMR resonances at positions C1 and C2, closest to the thiol group. On the basis of chemical shift comparison to the free ligands, the C1 and C2 positions were both found to undergo extensive line broadening and downfield shifts of 18 and 12 ppm, respectively. The changes in chemical shift upon coordination to AuNPs were consistent with strongly adsorbed organosulfur species.

Here, metal-specific NMR features were helpful in clarifying the origin of these changes in chemical shift. For example, the observed chemical shifts could arise from coupling of the $^{13}\text{C}_1$ and $^{13}\text{C}_2$ resonances to the conduction electrons on the AuNP surface. However, the T_1 values did not exhibit a linear relationship with temperature. This lack of Korringa behavior indicated that the resonances experienced little, if any, Knight shift contribution to the observed NMR chemical shift. Further comparison to analogous diamagnetic Au(I)–thiolates showed similar changes in chemical shift at the C1 and C2 position to those observed in the nanoparticle system. Taken together, the absence of Korringa behavior and similarity to Au(I)–thiolate chemical shifts, ruled out a metallic contribution and suggested the origin of chemical shift change was from the presence of a Au–thiolate bond at the particle surface.

Once the origin of the chemical shift difference was assigned, the source of line broadening was evaluated. The fwhm of both the C1 and C2 resonances of the thiolate-capped AuNPs were both broadened significantly (fwhm = 1000–1300 Hz). As mentioned in Section 1.1, MAS techniques eliminate contributions from CSA as well as isotropic bulk magnetic susceptibility sources of broadening. Upon MAS, the line widths of C1 and C2 were reported to narrow only slightly, indicating that the contribution to the line broadening was the result of a distribution of isotropic chemical shifts. A hole burning experiment confirms the heterogeneous line broadening of C2, which is likely the result of a chemical shift distribution from chemisorption of the thiol on various crystallographic sites of the AuNPs. These distributions in ligand-particle bonding environments are then assigned to the impact of a highly faceted particle surface (i.e., different crystallographic facets produce distinct environments for ligand and metal nuclei) as well as deviations in particle shape. Likewise, crystallographic variation in chemisorption sites was also independently found to cause heterogeneous line broadening in ^{31}P and ^1H resonances on triphenylphosphine-capped

AuNPs ($d = 1.8$ nm), as determined by ^{31}P and ^1H hole-burning experiments.⁵³ Both studies indicate that changes in line width and chemical shift upon particle attachment are primarily the result of heterogeneous line broadening mechanisms from a distribution of chemical environments on various surface facets.

In both instances, NMR was able to provide unprecedented insight into the processes contributing to line broadening and chemical shift changes of the resonances closest to the ligand anchoring moiety on NMNPs. Further, there are notable cases in which NMR spectroscopy of the ligand shell may provide information about the chirality of the ligand arrangement or even the underlying particle itself. Using a combination of 1D and 2D solution phase ^1H NMR techniques, Jin, Gil and co-workers demonstrated that glutathione-terminated $\text{Au}_{25}(\text{SG})_{18}$ clusters exhibit two different types of surface thiolate binding modes, consistent with previous NMR spectroscopy and X-ray crystallography results for $\text{Au}_{25}(\text{SCH}_2\text{CH}_2\text{Ph})_{18}$.⁷³ Alterations in ^1H chemical shift as a result of underlying Au nanocluster chirality were also examined,⁷⁴ similar to methods used in traditional organic synthesis. In both cases, the ^1H NMR chemical shift behavior is sensitive to the surrounding electronic environment, which includes the electronic structure and bonding environment of the nucleus. Therefore, changes in the handedness of a molecule can be “felt” by neighboring spin positions and is observed as a change in chemical shift, making NMR observables valuable for assessing chirality or nonchirality of small, molecule-like nanoclusters.

In the case of small, noble metal clusters (<200 atoms) it is important to note that interesting and often unexpected magnetic properties can arise.⁷⁵ For example, Maran and co-workers have shown that paramagnetic $\text{Au}_{25}\text{L}_{18}$ clusters exhibiting -1 , 0 , and $+1$ charges show marked shifts in ^1H and ^{13}C NMR properties based on cluster charge ($\text{L} = \text{S}(\text{CH}_2)_2\text{Ph}$).⁷⁶ Depending on the overall diamagnetic or paramagnetic character of the cluster, it may be appropriate to characterize the material with both NMR and electron paramagnetic resonance (EPR) spectroscopies.⁷⁷

More advanced NMR techniques such as deuterium NMR spectroscopy can be used to enhance both spatial and chemical resolution in structure and dynamics studies of NMNP ligand shells. Unlike ^{13}C and ^1H NMR spectroscopies, ^2H NMR spectroscopy directly probes quadrupolar ^2H coupling, and in the case of many solids, the NMR spectrum is dominated by the ^2H quadrupolar interaction.^{13,78} ^2H quadrupolar coupling is a parameter that is a physical representation of the amplitude and symmetry of molecular motion present at each deuterated site, providing exceptional structural information. These methods are routinely exploited for polymeric materials⁷⁹ and similar approaches can be applied to study the structure and dynamics of the ligand shell of both phosphine-⁸⁰ and thiolate-capped NMNPs.⁶⁹

In one example, VT static ^2H ssNMR was used in combination with DSC and FTIR to study site-specifically deuterated (position 1 and 10–13) and perdeuterated (2–18) octadecanethiol-capped AuNPs. These particles were then used to study the molecular origin of several thermodynamic phenomena such as ligand shell melting transitions.⁶⁹ Here, Lennox and co-workers used ^2H NMR to show that alkanethiols attached to AuNP surfaces undergo rapid trans-gauche bond isomerization and axial chain rotation, consistent with observations deduced from previous ^{13}C and ^1H NMR studies (vide supra, Figure 6A,D). The phase transition

detected by DSC was found to arise from a thermally induced transformation from a predominantly trans chain conformation to a largely disordered state. ^2H NMR spectroscopy was able to definitively demonstrate that chain melting originates from a population of gauche bonds that begin in the chain termini and increasingly progress to the middle of the chain with increasing temperature (Figure 6C). However, monitoring the thermal behavior of ^2H resonances at position 1 indicated that conformational order is maintained adjacent to the anchoring sulfur atom. The detailed, molecular description that emerged from these studies was in good agreement with previously observed trends for octadecanethiols in 2D SAMs as well as lipid membrane systems and gave an unprecedented structural foundation for the emergent thermodynamic properties of alkanethiol SAMs on AuNPs.

3.2. Metal Nanoparticle Surface Chemistry: Adsorbed Gases.

In this section we highlight studies of gas adsorption onto substrates that evaluate the behavior of the gas, including location and geometry of binding sites as well as diffusion coefficients. These experiments are of particular interest to the catalytic community and have been used primarily to elucidate the structure and properties of NMNPs that lead to effective catalysts. In Section 3.3.3, we will address experiments that use adsorbed gases to probe the underlying properties of the metal nanoparticle core.

Pioneering studies on hydrogen adsorbed to a variety of NMNPs as well as an overview of several reactions including hydrogenation of benzene, methanation reactions, and the scission of C_2H_2 and C_2H_4 species on nanoparticle surfaces are covered in Slichter's 1986 review.⁴ The reader is referred to this review and the references therein for a comprehensive perspective on the seminal works in this field. Here, we focus on more recent advances using NMR spectroscopy to study adsorbed species on NMNP surfaces.

Using VT 1D and 2D ^1H NMR, Pruski and co-workers adsorbed hydrogen gas onto SiO_2 -supported RuNP catalysts and showed that three different species of hydrogen gas could be identified at the metal surface.⁸¹ One of the hydrogen species exhibited strong adsorption properties, while the other two showed high molecular mobility. These three species likely represented disassociated H species, weakly bound H_2 , and H_2 in rapid exchange with the environment. Further examination of the adsorption properties of deuterium on NP surfaces has clarified some ambiguity in proton dynamics and binding sites in these systems. For example, surface ^2H species have been observed, as well as deuterons within the metal NP itself and the presence of mobile and/or reactive hydrides on ligand-capped RuNP systems. Chaudret and co-workers were able to distinguish between different crystallographic adsorption sites on the NP surface (i.e., fcc vs hcp, bridge vs linear) by pairing experimentally observed ^2H NMR quadrupolar coupling constants and asymmetry parameters of $^2\text{H}_2(\text{g})$ adsorbed on RuNPs to the values predicted with DFT calculations.⁸² This combination can be extended to determine the effect of ^2H adsorption on co-adsorbates, including changes in ligand chemistry, differences in coverage saturation, or variation in metal surface structure.

NMR has also been used to directly monitor the diffusion of adsorbed gases on the surface of metal NPs. Early work included determining various binding sites and exchange of ^{13}CO on RhNPs supported on alumina⁸³ and ^{13}CO diffusion on PtNPs.⁴ Later, using VT ^{13}C and ^2H NMR spectroscopy, Oldfield, Wieckowski, and co-workers found that CO diffusion

on PtNPs followed Arrhenius behavior and extracted both an activation energy and pre-exponential factor (6.0 ± 0.4 kcal/mol and $1.1 \pm 0.6 \times 10^{-8}$ cm²/s, respectively).⁸⁴ The proposed mechanism for CO diffusion was exchange between different CO populations driven by a chemical potential gradient. This study introduced a new method to quantitatively correlate diffusion of surface adsorbates to catalytic activity and should be amenable to the study of other adsorbed species and metal surfaces.

In a related study, the authors used a combination of ¹³CO electrochemical NMR and cyclic voltammetry (CV) to investigate the origin of Ru promoted electro-oxidation of MeOH on PtRuNP catalysts.⁸⁵ NMR results revealed two different types of ¹³CO on the catalysts, one population on pure Pt sites and another population on Pt–Ru islands. Surprisingly, no exchange was observed between different CO populations, and these observations were supported by CV measurements. Detailed analysis of ¹³C chemical shift changes and Korringa behavior between the two CO populations suggested that Ru weakens the Pt–CO bond, resulting in increased CO oxidation rates. The combination of NMR spectroscopy and electrochemistry provided unprecedented insight into CO tolerance and promotion in bimetallic NP catalysts.

3.3. Metal Nanoparticle Core Characterization.

3.3.1. Nanoparticle Size. A basic property of any nanoparticle is its size. NMR is a useful tool to measure the hydrodynamic radius of metal nanoparticles and can provide an important complement to traditional nanoparticle sizing techniques, such as electron microscopy and DLS. Similar to DLS, NMR signal can be used to determine nanoparticle size via analysis of particle diffusion. Specifically, NMR uses pulsed-field gradient (PFG) techniques to extract diffusion coefficients of well-dispersed species in solution diffusing according to Brownian motion only. Under these conditions, the hydrodynamic size is calculated by rearranging the Stokes–Einstein equation:

$$D = \frac{k_B T}{6\pi\eta R_H} \quad (3)$$

where D is the diffusion coefficient, k_B is the Boltzmann constant, T is temperature, η is viscosity of the solvent, and R_H is the hydrodynamic radius of the diffusing species.

However, unlike DLS, NMR provides the added benefit of chemical resolution. In ¹H (or other nuclei of interest) DOSY, a pseudo-2D NMR experiment is performed that separates NMR signals according to their diffusion coefficient. Murray and co-workers presented one of the first accounts of ¹H DOSY to measure the hydrodynamic size of Au colloids⁸⁶ and extended this approach to systematically study the size dependent ¹H DOSY signatures of AuNPs with core sizes ranging from 1.5 to 5.2 nm.⁵¹ Here, the authors also noted a correlation between nanoparticle core size and the fwhm of the ¹H NMR spectra, which was a result of the slower molecular tumbling and reduced correlation time (and, hence, decreased T_2 values) for larger particle sizes. Using changes in NMR spectral breadth as a function of particle size may be particularly useful for systems that are not amenable for DOSY analysis, such as dendrimer-encapsulated nanoparticles.⁸⁷ It is worth noting that DOSY analysis can be combined with NOE techniques to use NMNPs as a platform for NMR-based chemosensing of small molecules in solution as reported by Mancin and co-workers.^{88,89}

Building upon earlier work, Kubiak and co-workers reported a convenient nanoparticle sizing technique using ¹H DOSY measurements in deuterated organic solvents.⁹⁰ The sizes measured with DOSY compared well with results obtained from TEM for AuNPs ranging in size from $d = 2$ –5 nm. Nanoparticle size distributions were extracted from the data using the continuous method CONTIN.⁹¹ An important contribution of this study is the use of an internal standard for the calibration of nanoparticle sizing. The use of an internal standard mitigates experimental error while simultaneously simplifying data processing. Here, an internal standard with both a well-defined hydrodynamic size and ¹H NMR resonances well-resolved from that of the nanoparticle ligand resonances is added to the sample before ¹H DOSY measurement. Common examples of internal standards include ferrocene for organic solvents and dioxane for aqueous media. During the experiment, the diffusion coefficients of both the internal standard and the nanoparticle-bound ligands are measured. The hydrodynamic radius of the nanoparticle can then be calculated from eq 4:

$$R_{NP} = \frac{D_{ref}}{D_{NP}} R_{ref} \quad (4)$$

where R_{NP} is the hydrodynamic radius of the nanoparticle, D_{ref} is the diffusion coefficient of the reference molecule as measured by ¹H DOSY, D_{NP} is the diffusion coefficient of the ligands bound to the nanoparticle as measured by ¹H DOSY, and R_{ref} is the known hydrodynamic radius of the reference molecule in the solvent of interest. The measurement of relative diffusion coefficients minimizes error from changes in sample temperature, viscosity, instruments, independent measurements, and fluctuations during data acquisition. In our laboratory, we have found that this method can be extended to measure the hydrodynamic size of a range of metal nanoparticle compositions in polar and nonpolar solvents, and that sizes obtained match well with those measured by TEM.^{92,93}

Further, we have also found that, by changing the chain length of capping ligand on the nanoparticle surface, we are able to tune and detect corresponding changes in hydrodynamic radius using ¹H DOSY. Likewise, Häkkinen and co-workers found that the apparent diffusion coefficient and hydrodynamic size of Au nanoclusters (144 and 102 atoms) capped with *p*-mercaptobenzoic acid (*p*MBA) in aqueous solution depends strongly on the counterion of the deprotonated *p*MBA[–] capping ligand.⁹⁴ DFT calculations revealed that competing hydrogen bonding interactions and ion-pairing between the *p*MBA[–], Na⁺, NH₄⁺, acetic acid, and water molecules affected the hydrodynamic size of the Au nanoclusters.

Despite these successes, measuring nanoparticle size becomes more challenging and time-consuming with larger particle diameters due to the NMR line broadening effects observed from slower tumbling at larger sizes. It may be that ¹H DOSY is most useful at size ranges where alternate sizing techniques, such as TEM imaging, becomes less useful (due to both instrument and sample limitations). It is also important to note that NMR is a population-averaged technique, meaning that ¹H DOSY could introduce a bias toward larger particle sizes when performing sizing measurements, assuming that larger diameter particles contain more capping ligands than smaller ones. However, with these caveats in mind, the

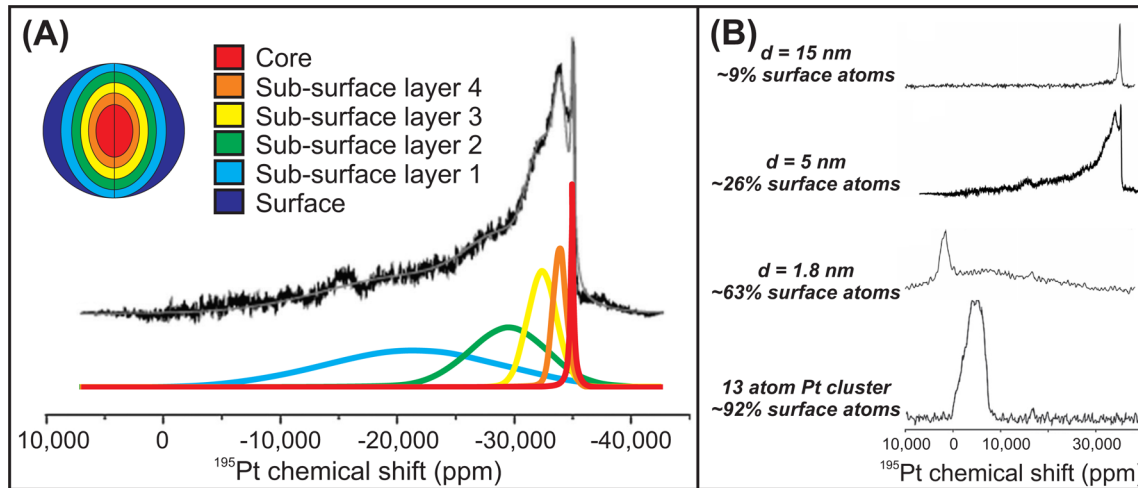


Figure 7. (A) Wideline ^{195}Pt NMR spectrum of 5 nm carbon-supported PtNPs showing deconvolution as a function of atom position. (B) Change in ^{195}Pt NMR line shape as a function of PtNP core diameter and % surface atoms. Adapted with permission from ref 115. Copyright 2013 Royal Society of Chemistry.

combination of ^1H DOSY, TEM, and UV-vis can provide robust and sometimes otherwise inaccessible information on the average size of metal nanoparticles.

3.3.2. Nanoparticle Core Properties Observed Using Metal Nuclei. Here, we discuss NMR spectroscopy of metal nuclei contained within the nanoparticle itself. These experiments reveal detail both about the nanoparticle physical architecture as well as its electronic structure. For a comprehensive discussion on the theory and history of metal NMR to study particles and clusters, we refer the readers to a classic review by van der Klink and Brom from 2000.⁵ Likewise, the quantum dot and metal oxide communities have leveraged direct NMR observation of nuclei that compose the nanomaterial to learn about details such as surface architecture⁹⁵ and particle electronic structure⁹⁶ as a function of size. For metals, ^{109}Ag ,^{97–101} ^{103}Rh ,¹⁰² and ^{63}Cu ^{103–106} NMR of small metal nanoparticles have all been reported, but ^{195}Pt is the most well-studied nucleus, because of favorable NMR properties such as relatively high natural abundance (33.8%) and moderate gyromagnetic ratio. Here, we focus on reports of ^{195}Pt NMR with the note that techniques outlined for Pt may be extended to other NMR active metal nuclei as both instrumentation and methodology continue to advance.

Although ^{195}Pt NMR had been used previously to study a range of PtNP systems,¹⁰⁷ Slichter and co-workers reported one of the first observations of size dependent spectral changes in ^{195}Pt NMR line shape as a function of metal core diameter.^{4,108,109} This exciting result was confirmed by van der Klink and co-workers who also reported a broad ^{195}Pt NMR line shape spanning 2.5 MHz at 8.5 T from surface to core resonances in the presence of additional adsorbates.^{110–112} Ab initio calculations suggested that the ^{195}Pt NMR shift in the surface Pt species compared to the core was the result of a gradual decrease in the d -like Fermi-level local density of states (E_f -LDOS) upon moving from the inside of the particle to its surface.¹¹³ Further, Slichter and co-workers found that ^{195}Pt NMR line shape was a function of particle size and adsorbate identity.¹⁰⁸ As particle size decreased, the ^{195}Pt NMR peak corresponding to bulk Pt metal also decreased. Likewise, when the particles were coated with adsorbates, a surface peak was observed in the region where diamagnetic ^{195}Pt species are typically observed. When the surface of the particles was

“cleaned” (heat treated to remove adsorbed molecules), the peak disappeared. Additionally, the frequency of the ^{195}Pt NMR surface peak was dependent upon the chemical identity of the adsorbate.

In order to extract more quantitative information from wide-line static ^{195}Pt NMR lineshapes, Bucher and co-workers developed a layer model,^{110,114} which assumes a pseudospherical particle shape, and each population-weighted layer of Pt atoms contributes to a specific NMR frequency (Figure 7A).¹¹⁵ In this model, the average Knight shift of a given layer, n , can be written as follows:

$$K_n = K_\infty + (K_0 - K_\infty)e^{(-n/m)} \quad (5)$$

where K_0 is the Knight shift of the surface, K_∞ is the Knight shift of bulk Pt, and m is the “healing length”. Here, the healing length is a probe of how strongly the more “molecule-like” surface is able to influence the metallic Knight shift of the interior Pt atoms. The healing length will vary with particle diameter, but Oldfield, Wieckowski, and co-workers have demonstrated that healing length can also depend on the electronegativity of adsorbates (vide infra).¹¹⁶

The difference in healing length can be seen in the shift of NMR frequency as a function of PtNP core diameter (Figure 7B). As the population of surface atoms increases, the population of surface species present in the spectrum increases accordingly. Likewise, to examine the influence of Pt core diameter ($d \approx 1\text{--}5$ nm) on catalytic behavior, Watanabe, Oldfield, Wieckowski, and co-workers used ^{195}Pt NMR analysis to study the oxygen reduction reaction (ORR) in an electrochemical environment.¹¹⁷ Surprisingly, ^{195}Pt NMR line shape and T_1 relaxation analysis indicated that surface Pt atoms showed similar electronic structure, regardless of core size, and thus had negligible effect on ORR rate constants. This work indicated that the electronic structure of the surface Pt species alone may dictate catalytic behavior, rather than changes in particle size (it is important to note that at NP sizes where the number of surface atoms dominates the total atom population of the particle, these two effects (core size vs surface structure) may be indistinguishable).¹¹⁸

In addition to the influence of particle size on E_f -LDOS, the influence of particle surface chemistry has also been examined

using ^{195}Pt NMR. For example, comparison of ^{195}Pt NMR lineshapes, chemical shifts, and T_1 relaxation behavior of clean, K-, and Li-impregnated PtNP catalysts revealed that alkali salt-impregnation increased $E_{\text{f}}\text{-LDOS}$ at surface Pt sites by 10–15%.¹¹⁹ This result was in contrast to H_2 adsorption, which was shown to diminish $E_{\text{f}}\text{-LDOS}$ at Pt surface sites. The spatial resolution available with ^{195}Pt NMR analysis also indicated that the alkali salt adds to the surface of the PtNPs and does not diffuse to the particle interior. These data provided a structural basis for proposed mechanisms of alkali salt promotion in PtNP catalysts.

Holding PtNP core size constant ($d \approx 2.5$ nm), Oldfield, Wieckowski, and co-workers systematically investigated the influence of a variety of adsorbates (H, O, S, CN^- , CO, and Ru) on ^{195}Pt NMR figures of merit.¹¹⁶ Here, the authors found that the Knight shift of interior Pt atoms remained unchanged, regardless of surface chemistry. However, the Knight shift of the surface and subsurface Pt sites varied over $\sim 11\,000$ ppm and showed an increasing downfield shift as the electronegativity of the adsorbate increased. Similarly, in two independent reports, Pt atoms bound to organic capping ligands exhibited no Knight shift and did not show typical Korringa behavior, while Pt atoms at the core exhibited metallic properties.^{120,121}

Another class of relevant Pt-containing nanostructures that are particularly difficult to characterize are small multimetallic architectures ($d = 1\text{--}3$ nm) containing Pt and at least one other metal. In these materials, the number as well as the position of the constituent metal atoms are crucial to their optical, catalytic, and magnetic properties. Methods such as X-ray absorption techniques as well as ssNMR can provide comprehensive information on metal nanoparticle architectures. NMR has the advantage of being more accessible and therefore can provide real-time analysis of ongoing experiments. Especially in the case of ^{195}Pt NMR, the electronic structure at both the surface and core of the nanoparticle can be determined by direct observation of the metal nucleus as described in pure Pt NPs above.

One of the first reports of ^{195}Pt NMR to probe bimetallic nanoparticles investigated Pt–Rh NPs and correlated the results with metal segregation observed in EDS.¹²² Further investigations used ^{195}Pt NMR to understand the changes in $E_{\text{f}}\text{-LDOS}$ of catalytically active PVP-coated Pt–Pd nanoparticles. Here, van der Klink and co-workers showed that the $E_{\text{f}}\text{-LDOS}$ of the interior Pt atoms varied strongly with % Pt composition, similar to observations in bulk Pt–Pd alloys.¹²³ The authors suggested that the changes in $E_{\text{f}}\text{-LDOS}$ were also present at the surface of the NPs and were responsible for changes in catalytic behavior as a function of composition in Pt–Pd particles.

In a separate report, Oldfield, Wieckowski, and co-workers used a combination of TEM, electrochemistry, and ^{195}Pt NMR spectroscopy to investigate the effect of heat treatment on bimetallic Pt–Ru nanoparticle alloys ($d = 2\text{--}3$ nm).^{85,124} Upon heat treatment at 600 °C, the ^{195}Pt NMR signal of Pt–Ru NPs shifted upfield, consistent with Pt migration to the interior of the particle.⁸⁵ This structural change resulted in a decrease in catalytic activity and was also consistent with a decrease in the number of Pt atoms on the surface of the NP. When the original sample was instead subjected to heat treatment at 220 °C in $\text{H}_2(\text{g})$, CO tolerance and methanol oxidation reactivity both increased, consistent with increased metallic Ru at the particle surface. At the same time, ^{195}Pt NMR resonances exhibited a change in Korringa product, $T_1\text{T}$, consistent with a

decrease in $E_{\text{f}}\text{-LDOS}$ of the Pt. Taken together, the changes in catalytic behavior and ^{195}Pt NMR properties led to the proposal of a Ru-rich core with a Pt–Ru alloy overlayer as a result of heat treatment at 220 °C in $\text{H}_2(\text{g})$. Later, Tong and co-workers expanded this approach to include ^{195}Pt NMR shift analysis for spatial distribution of Pt atoms in Pt–Ru nanoparticle alloys¹²⁵ as well as to probe electronic structure in other bimetallic compositions, including Pt–Au NPs.¹²⁶

Recently, Hanna and co-workers investigated a series of Pt_3X (where X = Sn, Al, Sc, Nb, Ti, Hf, and Zr) bimetallic nanoparticles with ^{195}Pt NMR spectroscopy.¹¹⁵ Here, the authors also used ssNMR analysis of the heteronuclei present in the Pt_3X alloys, which provided multielement information comparable to powder X-ray diffraction (XRD) techniques (XRD was also performed and correlated to the NMR results). Multinuclear NMR comparison with XRD facilitated assessment of bimetallic NP composition, size, relative order/disorder, and electronic structure. This study highlights the insight that can be achieved by combining NMR techniques with traditional materials characterization tools.

Despite its broad utility, routine acquisition of wide-line NMR spectra can be technically demanding. The inherent difficulty in acquiring ^{195}Pt NMR of Pt-containing nanoparticles lies in the fact that the static lineshapes often span several megahertz, making uniform broadband excitation challenging. Several approaches have been used to reconstruct ultra-wide-line patterns, including spin echo height spectroscopy (SEHS), variable offset cumulative spectroscopy (VOCS),¹²⁷ and field sweep Fourier transform (FSFT) spectroscopy.¹¹⁵ The development of methods such as wideband uniform rate smooth truncation—Carr–Purcell Meiboom–Gill (WURST-CPMG)¹²⁸—promise to greatly reduce the time and sensitivity burden associated with collecting ultra-wide-line spectra, while accurately replicating lineshapes. Importantly, the advent of broadband excitation and sensitivity enhancement techniques, such as FSFT and WURST-CPMG, suggest the opportunity to explore more exotic metal elements such as ^{105}Pd and ^{197}Au NMR as well as dramatically expand the characterization of Pt-containing NP systems.

3.3.3. Nanoparticle Core Properties Observed via Adsorbate Nuclei. Above, we describe the use of NMR to directly observe nuclei in the nanoparticle core. However, NMR of the adsorbate may also provide information about the morphology and electronic structure of the NP. For example, certain adsorbates such as ^{13}CO exhibit a Knight shift and corresponding Korringa behavior as a result of mixing between the adsorbate molecular orbitals and the transition metal d band.⁴

Slichter and co-workers conducted a large body of foundational work examining adsorbates on the surface of metal particles.^{4,129} In 1985, ^{13}CO adsorption on PtNPs was found to shift the ^{13}C resonance to much higher frequency (~ 200 ppm from the unbound CO resonance).¹³⁰ The authors suggested that this large shift was a Knight shift, and therefore the result of polarization of electron spins. This assignment was supported by the observation of Korringa behavior, and specifically the temperature dependent T_1 of the ^{13}CO molecule. Additionally, the $E_{\text{f}}\text{-LDOS}$ on the C atom was determined from electron spin resonance measurements on CO radicals. Slichter and co-workers went on to measure the T_1 behavior of ^{13}CO adsorbed on a variety of small metal particle compositions including Ru, Pd, Rh, Os, and Ir and were able to draw similar conclusions.⁴

A quantitative correlation between the Knight shift of chemisorbed ^{13}CO and the $E_{\text{f}}\text{-LDOS}$ on the surface of Pt and Pd nanoparticles was the subject of a later report by Oldfield, Wieckowski, and co-workers.¹³¹ In this work, the authors investigate the NMR properties of ^{13}CO adsorbed to PtNP and PdNP catalysts in an electrochemical environment. The data compared the ^{13}C Knight shift, $E_{\text{f}}\text{-LDOS}$ values from DFT calculations and NMR measurements of four systems: ^{13}CO adsorbed onto M_xCO clusters (where M = Pt or Pd),¹³¹ ^{13}CO adsorbed onto oxide-supported PtNPs in a dry environment,^{4,110} ^{13}CO adsorbed onto carbon-supported PtNPs in a wet electrochemical environment,¹³¹ and ^{13}CO adsorbed onto oxide-supported PdNPs in a dry environment (Figure 8).^{132,133} The linear relationship in Figure 8 was

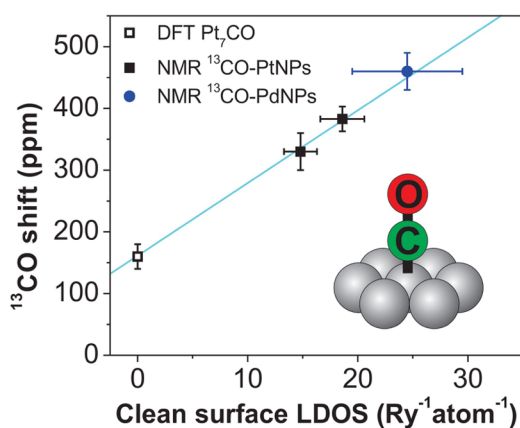


Figure 8. ^{13}CO Knight shift as a function of “clean surface” LDOS based on ab initio calculations of CO adsorbed on Pt₇ clusters (open black square) and experimental NMR measurements of ^{13}CO adsorbed on Pt (closed black squares) and Pd (closed blue circle) nanoparticle substrates. Adapted with permission from ref 131. Copyright 1999 American Chemical Society.

supported by trends in nanoparticle size as well as IR measurements of particle-bound CO.^{131,134} The authors suggested that the linear correlation between the Knight shift of chemisorbed CO, $K_{^{13}\text{CO}}$, and the clean $E_{\text{f}}\text{-LDOS}$ of the transition metal substrate followed the form:

$$K_{^{13}\text{CO}} = a \cdot \text{LDOS} \quad (6)$$

where $a \sim 11 (\pm 2)$ ppm/Ry $^{-1}$ atom $^{-1}$ for Pt and Pd.

While observation of the ^{195}Pt NMR resonance from the PtNP catalyst can serve as a direct probe of the $E_{\text{f}}\text{-LDOS}$ of the metal nanoparticle, direct NMR observation of metals such as ^{105}Pd nuclei remains challenging. However, ^{13}CO may be used as a probe of the underlying PdNP. Specifically, the authors measured the Knight shift and T_1 values of linear and bridge ^{13}CO adsorbed onto the surface of PdNPs as a function of temperature.¹³² These results are important because they suggest that the NMR behavior of the ligand nuclei bound to a metal surface can be used to probe the metal electronic properties, even in the case of NMR-silent metals. The correlation of ligand nuclei with metal core electronic properties dramatically expands the utility of NMR to understand the behavior of catalytic and photoactive nanomaterials.

Both theoretical¹³⁵ and experimental NMR⁶ studies provide evidence that, indeed, adsorbates other than ^{13}CO can probe the metallic and structural properties of nanoparticles. For

example, Kitagawa and co-workers used $^2\text{H}_2(\text{g})$ to examine morphology changes in bimetallic NPs. In these studies, the authors used ^2H NMR spectroscopy to distinguish between core–shell and alloyed architectures of Pd–Pt,¹³⁶ Pd–Au,¹³⁷ and Ag–Rh¹³⁸ nanoparticles, morphologies which could be tuned as a function of atomic composition.

Tong and co-workers used ^{77}Se NMR to examine the influence of selenol-terminated ligands on underlying AuNP electronic properties. In this case, results indicated changes in both the chemical shift and the temperature dependent T_1 relaxation rate of the Se nucleus, consistent with strong coupling to electrons on the Au surface.¹³⁹ The NMR behavior observed in this case is consistent with a possible Knight shift contribution to the ^{77}Se NMR resonance. Unfortunately, analogous ^{33}S NMR experiments are not suitable for routine assessment of thiol-binding environments because ^{33}S exhibits unfavorable NMR properties such as a moderate quadrupole moment ($-6.78 \times 10^{-30} \text{ m}^2$), low natural abundance (0.76%), and low gyromagnetic ratio ($2.06 \times 10^7 \text{ rad T}^{-1} \text{ s}^{-1}$). However, based on the work presented by Tong and co-workers, ^{77}Se NMR of selenol-capped nanoparticles is a promising alternative probe of the NMNP metallic properties.

4. USING NMR TO ASSESS NANOPARTICLE PERFORMANCE

Because of its broad accessibility and its ability to analyze NMNPs *in situ*, NMR may be uniquely well-suited to monitor NMNP performance in certain applications. Here, we give examples of how NMR spectroscopy can provide robust structure–function correlations between NMNP architecture and its utility in applications such as bioimaging and heterogeneous catalysis.

4.1. Magnetic Properties. NMR techniques can be used to measure figures of merit for magnetic resonance imaging (MRI) contrast agents. The principles that apply to metal nanoparticle systems are identical to other contrast agents and are not discussed in detail here. Briefly, in order to ascertain the efficacy of an MRI contrast agent, T_1 and T_2 relaxation rates of surrounding media are measured as a function of metal or nanoparticle concentration using standard inversion–recovery and CPMG pulse sequences, respectively. The slope of the resulting relationship between T_1 or T_2 relaxation rate vs concentration is referred to as the relaxivity value, r_1 or r_2 , respectively, which can be used to compare between different contrast agents.

In addition to MRI, NMR measurements can provide a fundamental understanding of the magnetic susceptibility in colloids. The NMR-based Evans’ method¹⁴⁰ is a particularly attractive technique to measure magnetic susceptibility because it can be used to rapidly evaluate the magnetic properties of NPs in solution (the entire colloid is analyzed), it does not require a large amount of material (~1 nmol NPs), and it is a relatively simple, widely accessible procedure (1D ^1H NMR acquisition, performed on any NMR instrument). Importantly, the Evans’ method is also more tolerant of surrounding diamagnetic materials appended to the NP surface (e.g., small molecule ligands), in contrast to other susceptibility measurements such as superconducting interference quantum device (SQUID) measurements.

In the Evans’ method, the mass magnetic susceptibility is measured by comparing the ^1H NMR chemical shift of a solution containing the magnetic colloid and a standard with that of the pure standard (if suitable, the solvent can serve as

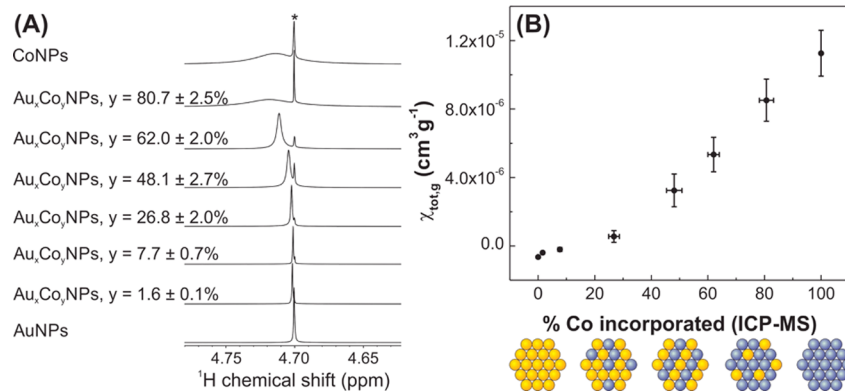


Figure 9. (A) Evans' method ¹H NMR spectra of the HDO peak in pure D₂O (asterisk) and the HDO peak in D₂O containing various colloidal compositions. (B) Mass susceptibility as a function of % Co incorporated in Au_xCo_yNP alloys, as measured from the Evans' method spectra in (A). Yellow circles = Au atoms. Blue circles = Co atoms. Adapted with permission from ref 93. Copyright 2014 Wiley-VCH Verlag GmbH & Co. KGaA.

the standard). The comparison can be made using a coaxial insert inside an NMR tube, with the inner tube containing pure standard and the outer tube containing both the standard and the colloid of interest. This experimental approach allows acquisition of both species in a single 1D ¹H NMR spectrum. The difference in ¹H NMR frequency between the standard in the colloidal solution and the pure standard is related to the total mass susceptibility by a modified Evans' method equation:¹⁴¹

$$\chi_{\text{tot,g}} = \frac{3\Delta f}{4\pi f m} + \chi_0 \quad (7)$$

Here, $\chi_{\text{tot,g}}$ is the total mass susceptibility, Δf is the frequency difference in Hz, f is the operating frequency of the spectrometer, m is the mass of magnetic species in 1 mL of solvent, and χ_0 is the mass susceptibility of the solvent. The Evans' method has been used to rapidly assess the magnetic properties of superparamagnetic metal oxides and inorganic complexes and has started to be used to evaluate the susceptibility of binary metal nanoparticles, including Au–Ni¹⁴² and Au–Co.⁹³

Chandler and co-workers used the Evans' method to determine the room-temperature, solution-phase magnetic susceptibility of Au–Ni nanoparticles ($d = 3$ nm) and also measured these values using SQUID measurements.¹⁴² In this study, temperature-dependent SQUID measurements >10 K were difficult to obtain because of the diamagnetic contribution from excess dendrimer template, alkanethiols, and residual solvent necessary to stabilize the bimetallic structures. Here, the Evans' method provided an alternative to measure the net magnetic susceptibility at room temperature without perturbing sample integrity.

Recently, we used the Evans' method to determine the composition-tunable magnetic properties of Au_xCo_yNPs as a function of % Co incorporated in the final NP.⁹³ By increasing the concentration of Co in the final NP, the mass susceptibility of the NPs was tunable from -3.9×10^{-7} to 112.6×10^{-7} cm³/g (Figure 9). All measurements were performed at room temperature, in D₂O, with nanoparticle quantities of ~ 1 nmol NPs. Spectral acquisition was typically complete within 30 s, allowing high throughput analysis of many samples and compositions with little demand on material quantity.

In the previously described analysis, the total mass susceptibility is comprised of both the diamagnetic and paramagnetic contribution. If the molecular weight, M , of the

nanoparticle is known, the paramagnetic contribution can be extracted by converting the mass susceptibility to molar susceptibility according to eq 8 and subtracting the diamagnetic contribution using Pascal's constants¹⁴³ (eq 9).

$$\chi_{\text{tot,mol}} = M\chi_{\text{tot,g}} \quad (8)$$

$$\chi_{\text{para,mol}} = \chi_{\text{tot,mol}} - \chi_{\text{dia,mol}} \quad (9)$$

$$\mu^{\text{eff}} = \sqrt{8\chi_{\text{para,mol}} T} \quad (10)$$

From here, the effective magnetic moment, μ^{eff} , per nanoparticle can be calculated according to eq 10, using elemental analysis of particle concentrations. However, figures of merit such as blocking temperature, saturation magnetization, and extent of hysteresis must be determined using alternate magnetic characterization techniques such as SQUID. Yet, because SQUID is technically more demanding than NMR, NMR measurements of magnetic properties are an attractive complement and/or alternative for many NMNP investigations, including rapid screening in materials development for applications such as data storage, bioimaging, and supercomputing.

4.2. Catalytic Behavior. In addition to providing rapid, high throughput information on the magnetic properties of NMNPs, NMR can also be used to explore catalytic behavior. Several examples in the literature use NMR to monitor reactions on metal nanoparticle catalysts, some of which were highlighted in Section 3.2. Recently, Tsang and co-workers have used NMR to monitor reactant turnover in heterogeneous catalysis, but have also correlated changes in ¹³C chemical shift of chemisorbed formic acid with catalytic figures of merit. Specifically, the authors found that ¹³C chemical shift of adsorbed formic acid was related to the work function of the surface and the specific activity for a variety of carbon supported and PVP-coated colloids with both monometallic and bimetallic core@shell compositions (Figure 10).¹⁴⁴

Previously, the authors provided evidence that ¹³C-labeled formic acid can probe the electronic properties of Ru particle surfaces.¹⁴⁵ In this study, the authors introduce an oxygen spacer between the ¹³C label and the particle surface and were able to eliminate the line broadening from Knight shift effects (e.g., those observed with ¹³CO probe molecules). This approach was extended to several other monometallic and bimetallic NP systems. For ¹³C-labeled formic acid adsorbed to PVP-coated PdNPs, four separate resonances were observed

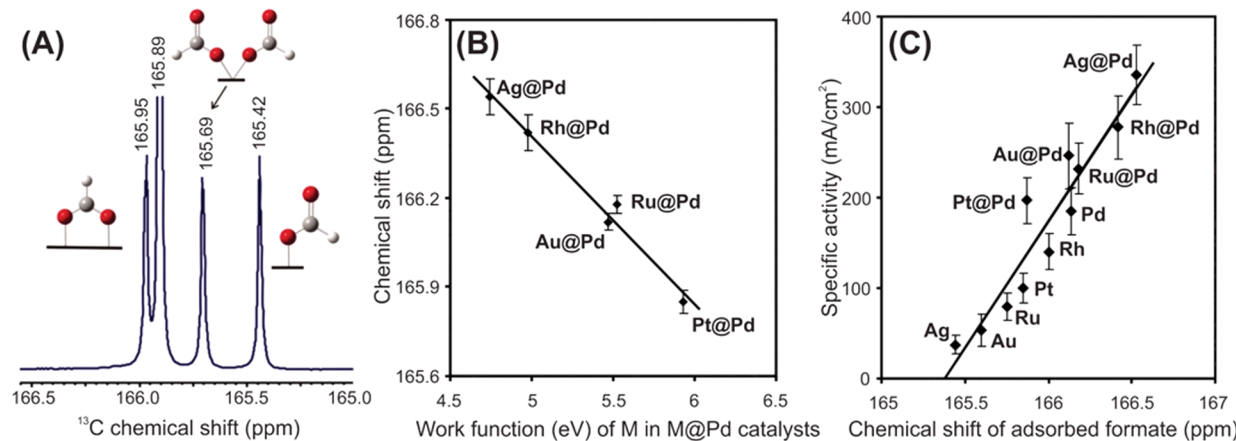


Figure 10. (A) Solution phase ^{13}C NMR spectrum of ^{13}C -labeled formic acid adsorbed to PVP-coated PdNPs. Distinct chemical shifts can be observed for each binding motif. (B) ^{13}C chemical shift of adsorbed bridging formic acid as a function of the workfunction of the core metal in core@shell, M@Pd catalysts. (C) Specific activity of various monometallic and bimetallic catalysts as a function of ^{13}C chemical shift of adsorbed bridging formate on the surface. Adapted with permission from ref 144. Copyright 2011 American Association for the Advancement of Science.

(Figure 10A). The peak at 165.89 ppm was assigned to weakly adsorbed formic acid that was in rapid exchange with free formic acid, leading to an average chemical shift. The remaining ^{13}C resonances, 165.42, 165.69, and 165.95 ppm, were assigned to monodentate, “multimonodentate” (see Figure 10A for molecular structure), and bridging formate adsorbed to the particle surface, respectively. ^{13}C NMR spectral assignment was correlated with FTIR spectroscopy results.

Remarkably, even in the presence of an oxygen spacer, DFT calculations suggested a significant degree of overlap of the 2s and 2p orbitals of the ^{13}C atom with metal *d*-electrons when formate was in a bridging conformation. Linear trends were observed between ^{13}C chemical shift of the bridging formate on the NP surface and the *d*-band center, work function (Figure 10B), and specific activity (Figure 10C) of the underlying catalysts. Similar trends were observed for a variety of metal types, particle sizes, and compositions, emphasizing the breadth of information gained by using NMR spectroscopy for routine NP performance evaluation.

5. OUTLOOK

From the work highlighted in this Perspective, it is clear that NMR spectroscopy has broad utility in the field of NMNPs, both in terms of the NMR techniques available and the NMNP properties measured.

Yet, it is also clear that there are challenges to capitalizing on this utility. The first barrier is low and largely logistical: many researchers trained and participating in nanoparticle studies are not also trained in the use of NMR as an analytical tool and likewise many experts in NMR spectroscopy are not active in nanomaterials research. This is changing rapidly as the utility of NMR in day-to-day nanochemistry work (e.g., particle sizing or ligand shell characterization) becomes apparent. Second, as mentioned previously, all NMR studies suffer from the inherent low sensitivity of Zeeman splitting. There are ongoing efforts to overcome this disadvantage with high field instrumentation, specialized hardware and pulse sequences,^{146,147} and techniques such as dynamic nuclear polarization.¹⁴⁸ Many of these strategies have already been used successfully in the field of structural biology, and it is likely that these advances can also be applied to the study of NMNPs. Finally, beyond basic 1 and 2D NMR techniques, both the technical and conceptual challenges

of NMR spectroscopy increase steeply. For example, experiments that combine electrochemistry and NMR within a single instrument are beyond the capabilities of many but the most expert NMR researchers. In these cases, we hope this Perspective will encourage expanded collaboration between the two disciplines so that, together, we can ask the most pressing scientific questions and answer them using the most accurate and efficient tools available.

Taken together, the work presented here demonstrates that NMR spectroscopy is a powerful complement to and sometimes an advantage over traditional materials characterization techniques for NMNPs. With a long history to build from, the future of NMR spectroscopy in the study of these systems is bright and should yield transformational insights into NMNP formation, structure, and performance.

■ AUTHOR INFORMATION

Corresponding Author

*E-mail: jem210@pitt.edu.

Notes

The authors declare no competing financial interest.

Biographies

Lauren E. Marbella earned her B.S. in biochemistry from Duquesne University in 2009, where she performed undergraduate research under the direction of Partha Basu. She earned her M.S. at the University of Pittsburgh under the direction of Megan M. Spence, studying peptide binding and morphology changes in lipid membranes using solid state NMR. In 2012, she joined the laboratory of Jill E. Millstone as a Ph.D. candidate investigating the formation and final particle characteristics of noble metal nanoparticles using magnetic resonance techniques.

Jill E. Millstone received her B.S. in Chemistry and English from Carnegie Mellon University in 2003, where she carried out undergraduate research in the laboratory of Richard D. McCullough. She completed her Ph.D. in materials chemistry in 2008 at Northwestern University under the direction of Chad Mirkin studying mechanisms of shape evolution in noble metal nanoparticles. She then joined the laboratories of Jean Fréchet and A. Paul Alivisatos as a postdoctoral researcher studying organic–inorganic photovoltaics. She joined the Chemistry department at the University of Pittsburgh in 2011 as an Assistant Professor, where her group focuses on the study of metal nanoparticle synthesis and surface chemistry.

■ ACKNOWLEDGMENTS

This work was supported by the National Science Foundation (CHE – 1253143), the Central Research Development Fund administered by the Office of Research and the University Research Council at the University of Pittsburgh, and the University of Pittsburgh. L.E.M. is supported by the Andrew Mellon Predoctoral Fellowship. We thank Michael J. Hartmann and Patrick J. Straney for helpful discussions.

■ REFERENCES

- (1) *Solid State NMR*. Chan, J. C. C., Ed.; Springer-Verlag: Berlin, 2012; Vol. 306.
- (2) Opella, S. J.; Marassi, F. M. *Chem. Rev.* **2004**, *104* (8), 3587.
- (3) Grey, C. P.; Dupré, N. *Chem. Rev.* **2004**, *104* (10), 4493.
- (4) Slichter, C. P. *Annu. Rev. Phys. Chem.* **1986**, *37* (1), 25.
- (5) van der Klink, J. J.; Brom, H. B. *Prog. Nucl. Magn. Reson. Spectrosc.* **2000**, *36* (2), 89.
- (6) Tong, Y. J.; Oldfield, E.; Wieckowski, A. *Anal. Chem.* **1998**, *70* (15), 518A.
- (7) Knight, W. D. *Phys. Rev.* **1949**, *76* (8), 1259.
- (8) Knight, W. D.; Kobayashi, S.-I. *Knight Shift. eMagRes*; John Wiley & Sons, Ltd.: 2007.
- (9) Bloembergen, N. *Can. J. Phys.* **1956**, *34* (12A), 1299.
- (10) Korringa, J. *Physica* **1950**, *16* (7–8), 601.
- (11) *Spin Dynamics: Basics of Nuclear Magnetic Resonance*, 2nd ed.; Levitt, M. H.; John Wiley & Sons Ltd.: Chichester, 2001.
- (12) Jameson, C. J.; Mason, J. The Chemical Shift. In *M multinuclear NMR*; Mason, J., Ed.; Plenum Press: New York, 1987.
- (13) *Solid State NMR Spectroscopy: Principles and Applications*; Duer, M. J., Ed.; Blackwell Science: Oxford, 2002.
- (14) Widdifield, C. M.; Schurko, R. W. *Concepts Magn. Reson., Part A* **2009**, *34A* (2), 91.
- (15) *Solid-State NMR in Materials Science: Principles and Applications*; Bakhmutov, V. I., Ed.; CRC Press: Boca Raton, 2011.
- (16) Brust, M.; Walker, M.; Bethell, D.; Schiffirin, D. J.; Whyman, R. J. *Chem. Soc., Chem. Commun.* **1994**, *7*, 801.
- (17) Goulet, P. J. G.; Lennox, R. B. *J. Am. Chem. Soc.* **2010**, *132* (28), 9582.
- (18) Li, Y.; Zaluzhna, O.; Xu, B.; Gao, Y.; Modest, J. M.; Tong, Y. J. *J. Am. Chem. Soc.* **2011**, *133* (7), 2092.
- (19) Li, Y.; Zaluzhna, O.; Tong, Y. J. *Langmuir* **2011**, *27* (12), 7366.
- (20) Brust, M.; Fink, J.; Bethell, D.; Schiffirin, D. J.; Kiely, C. J. *Chem. Soc., Chem. Commun.* **1995**, No. 16, 1655.
- (21) Whetten, R. L.; Khouri, J. T.; Alvarez, M. M.; Murthy, S.; Vezmar, I.; Wang, Z. L.; Stephens, P. W.; Cleveland, C. L.; Luedtke, W. D.; Landman, U. *Adv. Mater.* **1996**, *8* (5), 428.
- (22) Simpson, C. A.; Farrow, C. L.; Tian, P.; Billinge, S. J. L.; Huffman, B. J.; Harkness, K. M.; Cliffel, D. E. *Inorg. Chem.* **2010**, *49* (23), 10858.
- (23) Barngrover, B. M.; Aikens, C. M. *J. Phys. Chem. Lett.* **2011**, *2* (9), 990.
- (24) Mpourmpakis, G.; Caratzoulas, S.; Vlachos, D. G. *Nano Lett.* **2010**, *10* (9), 3408.
- (25) Stefanescu, D. M.; Glueck, D. S.; Siegel, R.; Wasylissen, R. E. *Langmuir* **2004**, *20* (24), 10379.
- (26) Turkevich, J.; Stevenson, P. C.; Hillier, J. *Discuss. Faraday Soc.* **1951**, *11* (0), 55.
- (27) Frens, G. *Nature* **1973**, *241* (105), 20.
- (28) Doyen, M.; Bartik, K.; Bruylants, G. *J. Colloid Interface Sci.* **2013**, *399* (0), 1.
- (29) Deboutière, P.-J.; Coppel, Y.; Behra, P.; Chaudret, B.; Fajerwerg, K. *Gold Bull.* **2013**, *46* (4), 291.
- (30) Ott, L. S.; Cline, M. L.; Deetlefs, M.; Seddon, K. R.; Finke, R. G. *J. Am. Chem. Soc.* **2005**, *127* (16), 5758.
- (31) Polte, J.; Tuaev, X.; Wuithschick, M.; Fischer, A.; Thuenemann, A. F.; Rademann, K.; Krahnert, R.; Emmerling, F. *ACS Nano* **2012**, *6* (7), 5791.
- (32) Jones, L. C.; Buras, Z.; Gordon, M. J. *J. Phys. Chem. C* **2012**, *116* (23), 12982.
- (33) Malliserry, S. K.; Gudat, D. *Dalton Trans.* **2010**, *39* (18), 4280.
- (34) Penner, G. H.; Li, W. *Inorg. Chem.* **2004**, *43* (18), 5588.
- (35) Liu, C. W.; Lin, Y.-R.; Fang, C.-S.; Latouche, C.; Kahalal, S.; Saillard, J.-Y. *Inorg. Chem.* **2013**, *52* (4), 2070.
- (36) Pellechia, P. J.; Gao, J.; Gu, Y.; Ploehn, H. J.; Murphy, C. J. *Inorg. Chem.* **2004**, *43* (4), 1421.
- (37) Straney, P. J.; Marbella, L. E.; Andolina, C. M.; Nuhfer, N. T.; Millstone, J. E. *J. Am. Chem. Soc.* **2014**, *136* (22), 7873.
- (38) Ismail, I. M.; Kerrison, S. J. S.; Sadler, P. J. *J. Chem. Soc., Chem. Commun.* **1980**, No. 23, 1175.
- (39) Gerber, W. J.; Murray, P.; Koch, K. R. *Dalton Trans.* **2008**, No. 31, 4113.
- (40) Hubbard, A. T.; Anson, F. C. *Anal. Chem.* **1966**, *38* (13), 1887.
- (41) Chen, C.; Kang, Y.; Huo, Z.; Zhu, Z.; Huang, W.; Xin, H. L.; Snyder, J. D.; Li, D.; Herron, J. A.; Mavrikakis, M.; Chi, M.; More, K. L.; Li, Y.; Markovic, N. M.; Somorjai, G. A.; Yang, P.; Stamenkovic, V. R. *Science* **2014**, *343* (6177), 1339.
- (42) Sun, S.; Murray, C. B.; Weller, D.; Folks, L.; Moser, A. *Science* **2000**, *287* (5460), 1989.
- (43) Anderson, N. C.; Hendricks, M. P.; Choi, J. J.; Owen, J. S. *J. Am. Chem. Soc.* **2013**, *135* (49), 18536.
- (44) Hens, Z.; Martins, J. C. *Chem. Mater.* **2013**, *25* (8), 1211.
- (45) Tagliazucchi, M.; Tice, D. B.; Sweeney, C. M.; Morris-Cohen, A. J.; Weiss, E. A. *ACS Nano* **2011**, *5* (12), 9907.
- (46) Valdez, C. N.; Schimpf, A. M.; Gamelin, D. R.; Mayer, J. M. *ACS Nano* **2014**, *8* (9), 9463.
- (47) Gentilini, C.; Franchi, P.; Mileo, E.; Polizzi, S.; Lucarini, M.; Pasquato, L. *Angew. Chem., Int. Ed.* **2009**, *48* (17), 3060.
- (48) McIntosh, C. M.; Esposito, E. A.; Boal, A. K.; Simard, J. M.; Martin, C. T.; Rotello, V. M. *J. Am. Chem. Soc.* **2001**, *123* (31), 7626.
- (49) Wang, G.; Guo, R.; Kalyuzhny, G.; Choi, J.-P.; Murray, R. W. *J. Phys. Chem. B* **2006**, *110* (41), 20282.
- (50) Zaupa, G.; Mora, C.; Bonomi, R.; Prins, L. J.; Scrimin, P. *Chem.—Eur. J.* **2011**, *17* (17), 4879.
- (51) Hostetler, M. J.; Wingate, J. E.; Zhong, C.-J.; Harris, J. E.; Vachet, R. W.; Clark, M. R.; Londono, J. D.; Green, S. J.; Stokes, J. J.; Wignall, G. D.; Glish, G. L.; Porter, M. D.; Evans, N. D.; Murray, R. W. *Langmuir* **1998**, *14* (1), 17.
- (52) Zelakiewicz, B. S.; de Dios, A. C.; Tong, Y. J. *J. Am. Chem. Soc.* **2002**, *125* (1), 18.
- (53) Sharma, R.; Holland, G. P.; Solomon, V. C.; Zimmermann, H.; Schiffenhaus, S.; Amin, S. A.; Buttry, D. A.; Yarger, J. L. *J. Phys. Chem. C* **2009**, *113* (37), 16387.
- (54) Smith, A. M.; Marbella, L. E.; Johnston, K. A.; Hartmann, M. J.; Crawford, S. E.; Kozycz, L. M.; Seferos, D. S.; Millstone, J. E. *Anal. Chem.* **2015**, DOI: 10.1021/ac504081k.
- (55) Barantin, L.; Le Pape, A.; Akoka, S. *Magn. Reson. Med.* **1997**, *38* (2), 179.
- (56) Zhou, H.; Du, F.; Li, X.; Zhang, B.; Li, W.; Yan, B. *J. Phys. Chem. C* **2008**, *112* (49), 19360.
- (57) Calzolai, L.; Franchini, F.; Gilliland, D.; Rossi, F. *Nano Lett.* **2010**, *10* (8), 3101.
- (58) Guarino, G.; Rastrelli, F.; Mancin, F. *Chem. Commun.* **2012**, *48* (10), 1523.
- (59) Guarino, G.; Rastrelli, F.; Scrimin, P.; Mancin, F. *J. Am. Chem. Soc.* **2012**, *134* (17), 7200.
- (60) Solomon, I. *Phys. Rev.* **1955**, *99* (2), 559.
- (61) Bloembergen, N. *J. Chem. Phys.* **1957**, *27* (2), 572.
- (62) Liu, X.; Yu, M.; Kim, H.; Mameli, M.; Stellacci, F. *Nat. Commun.* **2012**, *3*, 1182.
- (63) Gullion, T.; Schaefer, J. *J. Magn. Reson.* **1989**, *81* (1), 196.
- (64) Abraham, A.; Mihaliuk, E.; Kumar, B.; Legleiter, J.; Gullion, T. *J. Phys. Chem. C* **2010**, *114* (42), 18109.
- (65) Abraham, A.; Ilott, A. J.; Miller, J.; Gullion, T. *J. Phys. Chem. B* **2012**, *116* (27), 7771.
- (66) Badia, A.; Lennox, R. B.; Reven, L. *Acc. Chem. Res.* **2000**, *33* (7), 475.

- (67) Soederlind, E.; Stilbs, P. *Langmuir* **1993**, *9* (7), 1678.
- (68) Badia, A.; Gao, W.; Singh, S.; Demers, L.; Cuccia, L.; Reven, L. *Langmuir* **1996**, *12* (5), 1262.
- (69) Badia, A.; Cuccia, L.; Demers, L.; Morin, F.; Lennox, R. B. *J. Am. Chem. Soc.* **1997**, *119* (11), 2682.
- (70) Schmitt, H.; Badia, A.; Dickinson, L.; Reven, L.; Lennox, R. B. *Adv. Mater.* **1998**, *10* (6), 475.
- (71) Fiurasek, P.; Reven, L. *Langmuir* **2007**, *23* (5), 2857.
- (72) Badia, A.; Demers, L.; Dickinson, L.; Morin, F. G.; Lennox, R. B.; Reven, L. *J. Am. Chem. Soc.* **1997**, *119* (45), 11104.
- (73) Wu, Z.; Gayathri, C.; Gil, R. R.; Jin, R. *J. Am. Chem. Soc.* **2009**, *131* (18), 6535.
- (74) Qian, H.; Zhu, M.; Gayathri, C.; Gil, R. R.; Jin, R. *ACS Nano* **2011**, *5* (11), 8935.
- (75) Nealon, G. L.; Donnio, B.; Greget, R.; Kappler, J.-P.; Terazzi, E.; Gallani, J.-L. *Nanoscale* **2012**, *4* (17), 5244.
- (76) Venzo, A.; Antonello, S.; Gascón, J. A.; Guryanov, I.; Leapman, R. D.; Perera, N. V.; Sousa, A.; Zamuner, M.; Zanella, A.; Maran, F. *Anal. Chem.* **2011**, *83* (16), 6355.
- (77) Dainese, T.; Antonello, S.; Gascón, J. A.; Pan, F.; Perera, N. V.; Ruzzi, M.; Venzo, A.; Zoleo, A.; Rissanen, K.; Maran, F. *ACS Nano* **2014**, *8* (4), 3904.
- (78) Chandrasekhar, N. *Spin-1 NMR*; Springer: Berlin, 1996.
- (79) Schmidt-Rohr, K.; Rawal, A.; Fang, X.-W. *J. Chem. Phys.* **2007**, *126*, 054701.
- (80) Sharma, R.; Taylor, R. E.; Bouchard, L.-S. *J. Phys. Chem. C* **2011**, *115* (8), 3297.
- (81) Engelke, F.; Bhatia, S.; King, T. S.; Pruski, M. *Phys. Rev. B* **1994**, *49* (4), 2730.
- (82) Pery, T.; Pelzer, K.; Bunkowsky, G.; Philippot, K.; Limbach, H.-H.; Chaudret, B. *ChemPhysChem* **2005**, *6* (4), 605.
- (83) Duncan, T. M.; Yates, J. T.; Vaughan, R. W. *J. Chem. Phys.* **1980**, *73* (2), 975.
- (84) Kobayashi, T.; Babu, P. K.; Gancs, L.; Chung, J. H.; Oldfield, E.; Wieckowski, A. *J. Am. Chem. Soc.* **2005**, *127* (41), 14164.
- (85) Babu, P. K.; Kim, H. S.; Kuk, S. T.; Chung, J. H.; Oldfield, E.; Wieckowski, A.; Smotkin, E. S. *J. Phys. Chem. B* **2005**, *109* (36), 17192.
- (86) Terrill, R. H.; Postlethwaite, T. A.; Chen, C.-h.; Poon, C.-D.; Terzis, A.; Chen, A.; Hutchison, J. E.; Clark, M. R.; Wignall, G.; Londono, J. D.; Superfine, R.; Falvo, M.; Johnson, C. S., Jr.; Samulski, E. T.; Murray, R. W. *J. Am. Chem. Soc.* **1995**, *117* (50), 12537.
- (87) Gomez, M. V.; Guerra, J.; Myers, V. S.; Crooks, R. M.; Velders, A. H. *J. Am. Chem. Soc.* **2009**, *131* (41), 14634.
- (88) Perrone, B.; Springhetti, S.; Ramadori, F.; Rastrelli, F.; Mancin, F. *J. Am. Chem. Soc.* **2013**, *135* (32), 11768.
- (89) Salvia, M.-V.; Ramadori, F.; Springhetti, S.; Diez-Castellnou, M.; Perrone, B.; Rastrelli, F.; Mancin, F. *J. Am. Chem. Soc.* **2015**, *137* (2), 886.
- (90) Canzi, G.; Mrse, A. A.; Kubiak, C. P. *J. Phys. Chem. C* **2011**, *115* (16), 7972.
- (91) Provencher, S. W. *Comput. Phys. Commun.* **1982**, *27* (3), 229.
- (92) Andolina, C. M.; Dewar, A. C.; Smith, A. M.; Marbella, L. E.; Hartmann, M. J.; Millstone, J. E. *J. Am. Chem. Soc.* **2013**, *135* (14), 5266.
- (93) Marbella, L. E.; Andolina, C. M.; Smith, A. M.; Hartmann, M. J.; Dewar, A. C.; Johnston, K. A.; Daly, O. H.; Millstone, J. E. *Adv. Funct. Mater.* **2014**, *24* (41), 6532.
- (94) Salorinne, K.; Lahtinen, T.; Malola, S.; Koivisto, J.; Häkkinen, H. *Nanoscale* **2014**, *6* (14), 7823.
- (95) Lovingood, D. D.; Achey, R.; Paravastu, A. K.; Strouse, G. F. *J. Am. Chem. Soc.* **2010**, *132* (10), 3344.
- (96) Cadars, S.; Smith, B. J.; Epping, J. D.; Acharya, S.; Belman, N.; Golani, Y.; Chmelka, B. F. *Phys. Rev. Lett.* **2009**, *103* (13), 136802.
- (97) Bercier, J. J.; Jirousek, M.; Graetzel, M.; van der Klink, J. J. *J. Phys.: Condens. Matter* **1993**, *5* (44), L571.
- (98) Mastikhin, V. M.; Mudrakovskiy, I. L.; Goncharova, S. N.; Balzhinimaev, B. S.; Noskova, S. P.; Zaikovsky, V. I. *React. Kinet. Catal. Lett.* **1992**, *48* (2), 425.
- (99) Plischke, J. K.; Benesi, A. J.; Vannice, M. A. *J. Phys. Chem.* **1992**, *96* (9), 3799.
- (100) Son, K.; Jang, Z. *J. Korean Phys. Soc.* **2013**, *62* (2), 292.
- (101) Suits, B. H.; Siegel, R. W.; Liao, Y. X. *Nanostruct. Mater.* **1993**, *2* (6), 597.
- (102) Vuissoz, P. A.; Yonezawa, T.; Yang, D.; Kiwi, J.; van der Klink, J. J. *J. Chem. Phys. Lett.* **1997**, *264* (3–4), 366.
- (103) Kobayashi, S.; Takahashi, T.; Sasaki, W. *J. Phys. Soc. Jpn.* **1972**, *32* (5), 1234.
- (104) Tunstall, D. P.; Edwards, P. P.; Todd, J.; Williams, M. J. *J. Phys.: Condens. Matter* **1994**, *6* (9), 1791.
- (105) Williams, M. J.; Edwards, P. P.; Tunstall, D. P. *Faraday Discuss.* **1991**, *92* (0), 199.
- (106) Yee, P.; Knight, W. D. *Phys. Rev. B* **1975**, *11* (9), 3261.
- (107) Yu, I.; Gibson, A.; Hunt, E.; Halperin, W. *Phys. Rev. Lett.* **1980**, *44* (5), 348.
- (108) Rhodes, H. E.; Wang, P.-K.; Stokes, H. T.; Slichter, C. P.; Sinfelt, J. H. *Phys. Rev. B* **1982**, *26* (7), 3559.
- (109) Slichter, C. P. *Surf. Sci.* **1981**, *106* (1–3), 382.
- (110) Bucher, J.; van der Klink, J. J. *Phys. Rev. B* **1988**, *38* (16), 11038.
- (111) Bucher, J. P.; Buttet, J.; van der Klink, J. J.; Graetzel, M. *Surf. Sci.* **1989**, *214* (3), 347.
- (112) van der Klink, J. J.; Buttet, J.; Graetzel, M. *Phys. Rev. B* **1984**, *29* (11), 6352.
- (113) Weinert, M.; Freeman, A. *Phys. Rev. B* **1983**, *28* (11), 6262.
- (114) Bucher, J. P.; Buttet, J.; van der Klink, J. J.; Graetzel, M.; Newson, E.; Truong, T. B. *Colloids Surf.* **1989**, *36* (2), 155.
- (115) Rees, G. J.; Orr, S. T.; Barrett, L. O.; Fisher, J. M.; Houghton, J.; Spikes, G. H.; Theobald, B. R. C.; Thompsett, D.; Smith, M. E.; Hanna, J. V. *Phys. Chem. Chem. Phys.* **2013**, *15* (40), 17195.
- (116) Tong, Y. J.; Rice, C.; Wieckowski, A.; Oldfield, E. *J. Am. Chem. Soc.* **2000**, *122* (48), 11921.
- (117) Yano, H.; Inukai, J.; Uchida, H.; Watanabe, M.; Babu, P. K.; Kobayashi, T.; Chung, J. H.; Oldfield, E.; Wieckowski, A. *Phys. Chem. Chem. Phys.* **2006**, *8* (42), 4932.
- (118) Kleis, J.; Greeley, J.; Romero, N. A.; Morozov, V. A.; Falsig, H.; Larsen, A. H.; Lu, J.; Mortensen, J. J.; Dulak, M.; Thygesen, K. S.; Nørskov, J. K.; Jacobsen, K. W. *Catal. Lett.* **2011**, *141* (8), 1067.
- (119) Tong, Y. J.; Martin, G. A.; van der Klink, J. J. *J. Phys.: Condens. Matter* **1994**, *6* (36), L533.
- (120) Tong, Y. J.; Zelakiewicz, B. S.; Dy, B. M.; Pogozelski, A. R. *Chem. Phys. Lett.* **2005**, *406* (1–3), 137.
- (121) van der Putten, D.; Brom, H. B.; Witteveen, J.; de Jongh, L. J.; Schmid, G. Z. *Phys. D, At., Mol. Clusters* **1993**, *26* (1), 21.
- (122) Wang, Z.; Ansermet, J.-P.; Slichter, C. P.; Sinfelt, J. H. *J. Chem. Soc., Faraday Trans. 1* **1988**, *84* (11), 3785.
- (123) Tong, Y. J.; Yonezawa, T.; Toshima, N.; van der Klink, J. J. *J. Phys. Chem.* **1996**, *100* (2), 730.
- (124) Babu, P. K.; Kim, H. S.; Oldfield, E.; Wieckowski, A. *J. Phys. Chem. B* **2003**, *107* (31), 7595.
- (125) Danberry, A. L.; Du, B.; Park, I.-S.; Sung, Y.-E.; Tong, Y. J. *J. Am. Chem. Soc.* **2007**, *129* (45), 13806.
- (126) Atienza, D. O.; Allison, T. C.; Tong, Y. J. *J. Phys. Chem. C* **2012**, *116* (50), 26480.
- (127) Massiot, D.; Farnan, I.; Gautier, N.; Trumeau, D.; Trokiner, A.; Coutures, J. P. *Solid State Nucl. Magn. Reson.* **1995**, *4* (4), 241.
- (128) MacGregor, A. W.; O'Dell, L. A.; Schurko, R. W. *J. Magn. Reson.* **2011**, *208* (1), 103.
- (129) Wang, P. K.; Ansermet, J. P.; Rudaz, S. L.; Wang, Z.; Shore, S.; Slichter, C. P.; Sinfelt, J. H. *Science* **1986**, *234* (4772), 35.
- (130) Rudaz, S. L.; Ansermet, J.-P.; Wang, P.-K.; Slichter, C. P.; Sinfelt, J. H. *Phys. Rev. Lett.* **1985**, *54* (1), 71.
- (131) Tong, Y. J.; Rice, C.; Godbout, N.; Wieckowski, A.; Oldfield, E. *J. Am. Chem. Soc.* **1999**, *121* (13), 2996.
- (132) Becerra, L.; Slichter, C.; Sinfelt, J. *Phys. Rev. B* **1995**, *52* (15), 11457.
- (133) MacDonald, A.; Daams, J.; Vosko, S.; Koelling, D. *Phys. Rev. B* **1981**, *23* (12), 6377.

- (134) Rice, C.; Tong, Y. J.; Oldfield, E.; Wieckowski, A.; Hahn, F.; Gloaguen, F.; Léger, J.-M.; Lamy, C. *J. Phys. Chem. B* **2000**, *104* (24), 5803.
- (135) Hammer, B.; Morikawa, Y.; Nørskov, J. *Phys. Rev. Lett.* **1996**, *76* (12), 2141.
- (136) Kobayashi, H.; Yamauchi, M.; Kitagawa, H.; Kubota, Y.; Kato, K.; Takata, M. *J. Am. Chem. Soc.* **2010**, *132* (16), 5576.
- (137) Kobayashi, H.; Yamauchi, M.; Ikeda, R.; Kitagawa, H. *Chem. Commun.* **2009**, No. 32, 4806.
- (138) Kusada, K.; Yamauchi, M.; Kobayashi, H.; Kitagawa, H.; Kubota, Y. *J. Am. Chem. Soc.* **2010**, *132* (45), 15896.
- (139) Zelakiewicz, B. S.; Yonezawa, T.; Tong, Y. J. *J. Am. Chem. Soc.* **2004**, *126* (26), 8112.
- (140) Evans, D. F. *J. Chem. Soc.* **1959**, No. 0, 2003.
- (141) Live, D. H.; Chan, S. I. *Anal. Chem.* **1970**, *42* (7), 791.
- (142) Auten, B. J.; Hahn, B. P.; Vijayaraghavan, G.; Stevenson, K. J.; Chandler, B. D. *J. Phys. Chem. C* **2008**, *112* (14), 5365.
- (143) Bain, G. A.; Berry, J. F. *J. Chem. Educ.* **2008**, *85* (4), 532.
- (144) Tedsree, K.; Chan, C. W. A.; Jones, S.; Cuan, Q.; Li, W.-K.; Gong, X.-Q.; Tsang, S. C. E. *Science* **2011**, *332* (6026), 224.
- (145) Tedsree, K.; Kong, A. T. S.; Tsang, S. C. *Angew. Chem., Int. Ed.* **2009**, *48* (8), 1443.
- (146) Hanna, J. V.; Smith, M. E. *Solid State Nucl. Magn.* **2010**, *38* (1), 1.
- (147) Schurko, R. W. *Acc. Chem. Res.* **2013**, *46* (9), 1985.
- (148) Ni, Q. Z.; Daviso, E.; Can, T. V.; Markhasin, E.; Jawla, S. K.; Swager, T. M.; Temkin, R. J.; Herzfeld, J.; Griffin, R. G. *Acc. Chem. Res.* **2013**, *46* (9), 1933.